

Simulating multi-wavelength observations from low-resolution spectrographs



Lasse Leth Skovsgaard Berthelsen

Master's Thesis in Astronomy
December 2020

SUPERVISOR: HANS KJELDSEN
Co-SUPERVISOR: VICTORIA ANTOCI

DEPARTMENT OF PHYSICS AND ASTRONOMY
AARHUS UNIVERSITY

SIMULATING MULTI-WAVELENGTH
OBSERVATIONS FROM
LOW-RESOLUTION SPECTROGRAPHS



LASSE LETH SKOVSGAARD BERTHELSSEN
201504594

MASTER'S THESIS IN ASTRONOMY
DECEMBER 2020

SUPERVISOR: HANS KJELDSEN
Co-SUPERVISOR: VICTORIA ANTOCI

DEPARTMENT OF PHYSICS AND ASTRONOMY
AARHUS UNIVERSITY

Colophon

Simulating multi-wavelength observations from low-resolution spectrographs

Master's thesis by Lasse Leth Skovsgaard Berthelsen. Written under supervision by Prof. Hans Kjeldsen, Department of Physics and Astronomy, Aarhus University.

Front illustration: A spectrum image generated using the HIDRA script presented in this thesis.

Back illustration: A convolved PSF and jitter image, created with the *psf_maker* and *func_jitter* functions.

This colophon disclaimer is intentionally left blank.

Typeset by the author with L^AT_EX and the memoir document class, using Linux Libertine and Linux Biolinum.

Printed at Aarhus University

Abstract

Objective: Spectroscopic investigation of exoplanetary atmospheres from space-borne platforms are currently only done by large-scale missions. Prior to manufacturing a small-platform space observatory, it is desirable to evaluate the capabilities of a given setup. The main focus of this thesis is thus to create and test a simple simulator for low-resolution spectrographs.

Method: A modular Python3-script called Hyperspectral Instrument Data Resemblance Algorithm (HIDRA) was created and all of its functionalities were thoroughly tested with sensible input parameters. This simulator can include a number of various effects, such as spacecraft jitter or CCD sub-pixel variation.

Results: A sample case were given, where externally supplied input parameters were used to evaluate a specific setup. It was concluded that the setup would be able to detect the atmosphere of the exoplanet in the theoretical stellar system, if the slit-design of the setup were swapped for a slit-less grism setup. The spacecraft jitter was deemed to be the primary cause of variations and errors in the test.

Future work: HIDRA can be improved in many ways, especially concerning the computation-time of a simulation. Higher spectral resolution and error handling, are two other key features to add in the near future.

Acknowledgements

While working on this thesis, many people have helped and supported me. Hans Kjeldsen and Vichi Antoci, my supervisor and co-supervisor, have helped me immensely in every aspect of the work process, from coding issues and bug-fixing, to finding sources and type-setting citations. A great thanks goes to them for helping me so much.

My fellow students and office-mates have helped me keep my sanity during the troubled times when my code was buggy or not working, and the many coffee-breaks and banter kept the negative thoughts at bay. Thank you to all of my friends at the university, especially Dina, Hasse, Sidsel, Line, and Christine.

My sister deserves the greatest and deepest gratitude, as she almost single-handedly saved my entire project. She helped correct my poor grammar and assisted me with the layout of thesis. She made me food during some of the more stressful nights and gave me tons of feedback throughout the entirety of my studies. Words cannot describe how grateful I am.

A word of gratitude should also be given to my fellow dorm-mates, who helped get my mind off work with board-games, movie-nights, and such. One could not ask for better people to live with.

I would also like to give thanks to my parents, for their continued support despite not always understanding the frustrations of my studies. I am, and will always be grateful for their support.

Lastly I would like to thank everyone who touched upon my life during these last 5½ years at the university. So many experiences to be had with all of these people have made my time at the university truly memorable.

Contents

Acronyms	1
1 Introduction and motivation	3
2 Exoplanets – the science case	5
2.1 Intermediate-mass stars	5
2.2 Observing exoplanets and their atmospheres	8
3 Satellites	15
3.1 Space environment	16
3.2 ADCS, spacecraft jitter	19
4 Spectroscopy & Optics	21
4.1 Spectrometers	21
4.2 Graded Prisms – Grisms	23
4.3 Hyperspectral imaging	24
4.4 Point Spread Function	25
5 Theory of Charge-Coupled Devices	29
5.1 CCD operation	29
5.2 Flat field, dark current & bias	30
5.3 CCD gain & non-linearity	32
5.4 Charge Transfer Efficiency	33
5.5 Sub-pixel structure	34
5.6 CMOS detectors	34
6 Simulator	35
6.1 Input format and units	37
6.2 Simulator modules	40
6.3 Auxiliary functions	45
7 Simulator testing	49
7.1 Input interpolator test	49

7.2	Convolution of PSF and jitter	50
7.3	Dispersion test	51
7.4	Exposure time	53
7.5	Sub-pixel to pixel summing	54
7.6	Concluding remarks on testing the simulator	55
8	Simulating a spectrograph	57
8.1	Simulator inputs	57
8.2	Method, results and discussion	59
9	Future improvements	69
10	Conclusion	73
	Bibliography	75

Acronyms

ADCS Attitude Determination and Control System.

CCD charge-coupled device.

CMOS complementary metal–oxide–semiconductor.

CTE charge transfer efficiency.

FWC full well capacity.

HIDRA Hyperspectral Instrument Data Resemblance Algorithm.

HST Hubble Space Telescope.

IR infrared.

LEO low-Earth orbit.

NIR near-infrared.

PSF Point Spread Function.

RV radial velocity.

RW reaction wheels.

TEC Total Efficiency Curve.

TESS Transiting Exoplanet Survey Satellite.



Introduction and motivation 1

“Somewhere, something incredible is waiting to be known.”

Carl Sagan

As so eloquently put by the late Carl Sagan, mankind has always been curious in almost every aspect of life. Some of our questions concern that of life and especially if life is possible elsewhere. This has been a major point of focus for many years of research and the question might be answered by exploring other planets. In recent years, planets orbiting other stars than our Sun were discovered – and they seem to be abundant and very varied in their sizes and orbital configurations.

For now, we have to search for ways to explore exoplanets other than visiting them, given the limited capabilities of current spaceflight. One such endeavour is the search for biosignatures – features of an exoplanet that might indicate the presence of life. Often this search is done by examining the spectral features (absorption lines) of the exoplanet’s atmosphere: A frequent example of a biosignature could be water vapour, as it is a universal requirement for life here on Earth.

In order to fully understand and investigate these atmospheres, full spectral coverage is needed as spectral features are found in most spectral bands. This requires observations made from space, as the atmosphere of the Earth is opaque in some spectral bands (such as the UV). To determine the data-quality and capabilities of such observations, computer-simulations are often implemented: That is the focus of this thesis; creating a simple, modular simulator capable of illustrating the end result of an exposure made with a spectrograph with a low spectral resolution, over a wide wavelength range.

Prior to explaining the simulator and its modules, the relevant background knowledge needed to understand the different aspects and reasoning behind the simulator is described.

In Chapter 2, the science case will be presented: Exoplanetary atmospheres and some of the basic principles behind detecting them is introduced. Following this, Chapter 3 will focus on satellites, which is one of the best platforms for observing the atmospheres of exoplanets. Some of the effects that can distort the quality of data are presented, such as spacecraft jitter. In Chapter 4, spectroscopy and the relevant aspect of optics are introduced. Chapter 5 will focus on the theory behind charge-coupled devices, including the structure and workings of these detectors.

After these chapters, the main product presented in this thesis will be explained: A simple modular simulator for detectors in low-resolution spectroscopy, called Hyperspectral Instrument Data Resemblance Algorithm (HIDRA). All of the necessary inputs and parameters are outlined at the beginning of Chapter 6, followed by a detailed walk-through of the entire simulation process. The modules and individual functions of the simulator are thoroughly tested and this is detailed in Chapter 7. In Chapter 8, a set of inputs, parameters and spectra are supplied for the purpose of testing the simulator in a user-defined scenario. The results of this simulation process are also contained within the chapter. After this, possible future improvements for the simulator are described in Chapter 9, followed by a general conclusion in Chapter 10.

Exoplanets – the science case 2

In the last two decades, humanity has found several thousands of exoplanets – planets that orbit a star other than the Sun. This has yielded a myriad of questions and puzzling phenomena: What kind of exoplanets exists and are some more common than others? Can some of them harbour life? Of the thousands of exoplanets found, they can mainly be categorized into three main groups, with several sub-classifications, etc. They are, in order of how many discovered so far: Neptune-like, terrestrial planets, and gas giants.¹ A particular sub-set of the gas giants, the so-called Hot Jupiters, are of particular interest as they orbit close to their host star. This makes them ideal targets for many detection methods that will be explained later in the chapter. Some of the questions posed earlier can be answered by studying the exoplanets closely, but in order to do that, careful study of their host star is also of the utmost importance. While many surveys have explored and studied exoplanets around low-mass and Solar-mass stars, the field of intermediate-mass stars is largely unexplored and for this reason, they are chosen as the area of interest.

2.1 Intermediate-mass stars

The specific type of star chosen as the area of interest is the intermediate-mass stars. They are similar to the Sun in their stellar evolutionary tracks but burn through their hydrogen much faster. This allows researchers to study their evolutionary track much better, than if only smaller stars were observed, as fewer lower-mass stars have reached the end of their evolution yet.

The evolutionary tracks of stars of different initial mass can be seen on Figure 2.1.

¹For the most recently updated numbers, see <https://exoplanets.nasa.gov/>

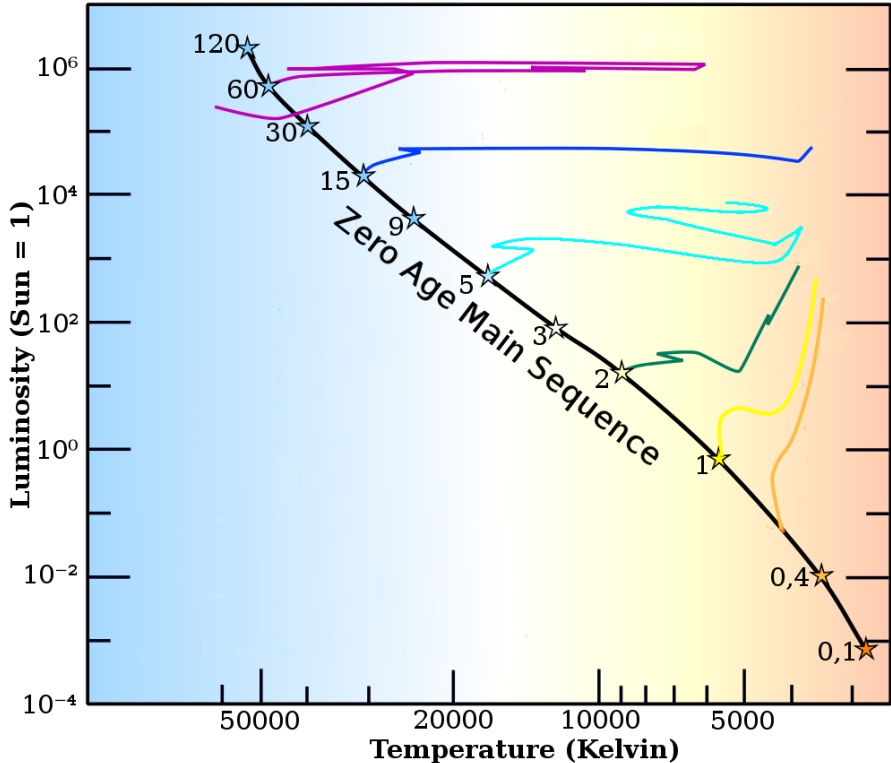


Figure 2.1: Hertzsprung-Russell diagram, showing the evolutionary tracks of stars with varying zero-age masses. For more massive stars, this evolution is faster.

Intermediate-mass stars are – as the name might suggest – in the middle of the possible mass-range of stars. In general, the lower mass-limit of stars is often considered the hydrogen burning mass limit of $\sim 0.075 M_{\odot}$ (e.g. Luhman [2012]). The upper limit is not precisely known, but few stars are known with masses larger than some hundreds of Solar-masses. A strict mass-range of intermediate-mass stars is hard to define, and in literature, the range varies from some $1-1.5 M_{\odot}$ to $8-10 M_{\odot}$ (e.g. Iben [1985], Iben and Renzini [1984], Karakas [2017], or Kippenhahn et al. [2012]). Some of the physical phenomena that set an intermediate-mass star apart from low-mass stars are the convective core (not present in Solar-like stars or smaller) and a lack of a core helium flash. The intermediate-mass stars instead have helium burning in the core for a relatively long time, called the helium main sequence (Kippenhahn et al. [2012]). The main difference between intermediate- and high-mass stars are the stellar remnant of such stars. Intermediate-mass stars end their

evolution as white dwarfs, while high-mass stars end in more exotic manners – supernovae and their subsequent compact objects, such as neutron stars. For a full overview of supernovae, see Alsabti and Murdin [2017].

Intermediate-mass stars are in broad terms short-lived versions of Sun-like stars. They are abundant in the solar neighbourhood – some of the brightest stars in the night sky are of this type, such as Sirius (α CMa) (Bond et al. [2017]), Vega (α Lyr) and Capella (α Aur).

These stars might harbour exoplanets (such as Pollux b, see Hatzes et al. [2006]), thus making these stars excellent candidates for studying exoplanets. Especially the exoplanetary atmospheres are of great interest: In the Solar system, most of the major planets have atmospheres and studying them have yielded great insight into the workings of those planets. Specifically studying the atmospheric composition can lead to interesting conclusions – water-vapour or other molecules might be detectable through their spectral absorption features. These can be thought of as potential biosignatures and could be an indication of the habitability of an exoplanet – leading to the “holy grail” of exoplanetary science: a habitable Earth-analogue. However, in order to study these atmospheres, the spectral absorption lines will have to be detectable and this requires observing in the corresponding wavelength band. For example, the spectral lines of water is often seen in the near-infrared (NIR) and microwave bands of the electromagnetic spectrum (a comprehensive database of spectral features of water, among many other molecules, can be found on the HITRAN database, see [HIT]). Other interesting molecules might have spectral features only in the UV or in the visible, so large spectral coverage is of key importance when studying exoplanetary atmospheres.

Detecting atmospheres and studying them over all wavelength ranges are, however, a great challenge – if not impossible – using current Earth-based facilities, as the atmosphere of the Earth is not fully transparent in all wavelengths, see Fig. 2.2.

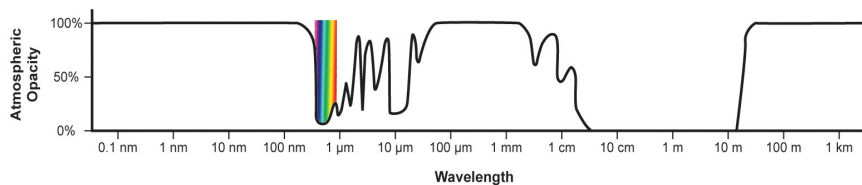


Figure 2.2: Illustration of the atmospheric opacity of the Earth. Visible, NIR, and radio waves can pass through the atmosphere almost unhindered, whereas most infrared (IR) and almost everything with a shorter wavelength than near-UV gets blocked.

This opacity means, that in order to get the full picture of exoplanetary atmospheres, researchers have to either make *in situ* measurements – currently only possible inside our Solar system – or use remote sensing from the atmosphere-free expanses of space. The latter will be explored further in Chapter 3. For now, the focus remains on the methods of discovering exoplanets and their atmospheres.

2.2 Observing exoplanets and their atmospheres

The difficulty in observing exoplanetary atmospheres lies in the contrast between the star and the exoplanet. Stars are very large compared to their orbiting planets, and while the stars radiate, planets only do so with their thermal radiation in IR – and often far too little to be detectable. Despite this major hurdle to surmount, there exists a wide variety in different detection methods, that will now be briefly explained.

2.2.1 Direct imaging

Exoplanets might reflect some light from their host star, but compared to the stellar light it is next to nothing – despite this, it is possible to directly detect exoplanets by blocking out the light from the host star (using a coronagraph²). Still, this method has only detected ~ 25 exoplanets, with fewer of those having detected atmospheres (e.g. Madhusudhan [2019]). Thus, other venues of detecting these exoplanetary atmospheres must be explored.

²Not to be confused with corona graph, i.e. the ones they keep showing on TV, anno 2020

2.2.2 Doppler spectroscopy

Another very useful technique is the radial velocity (RV) method, where orbital parameters of an exoplanet orbiting a star can be inferred by measuring the Doppler shift in spectral features of the stellar spectrum. While the technique is used for exoplanets in this context, it can be used for any binary system. A schematic illustration of the Doppler effect due to the orbit of the bodies around the barycenter can be seen on Figure 2.3. As the planet orbits the star, spectral features are observed. At the point where the planet only has a perpendicular velocity relative to the viewing angle, no change in the spectral lines is observed. However, if the planet is moving toward the observer, the star will be moving in the opposite direction (as it orbits the common barycenter of the system) and thus the light will be slightly red-shifted. The opposite then also holds when the planet is moving away and the stellar light is blue-shifted.

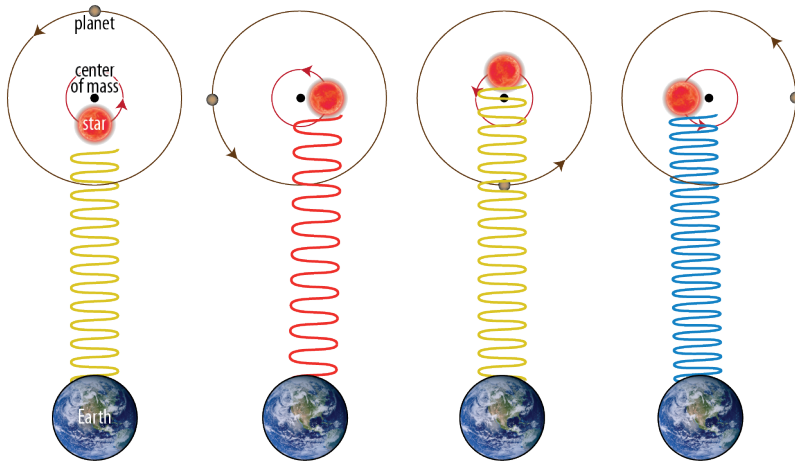


Figure 2.3: Illustration of Doppler shift in action. The movement of spectral absorption lines can then be compared to laboratory values. Adapted from <https://neid.psu.edu/what-is-neid/>.

As the exoplanet orbits its host star, the spectral lines observed will oscillate back and forth. The time it takes for one oscillation is equal to the orbital period of the planet (measured as the distance from peak-to-peak in Figure 2.4). The mass ratio of the system can be inferred by the observed semi-amplitudes of the system (the deviation from 0 m s^{-1} in v_r in Figure 2.4).

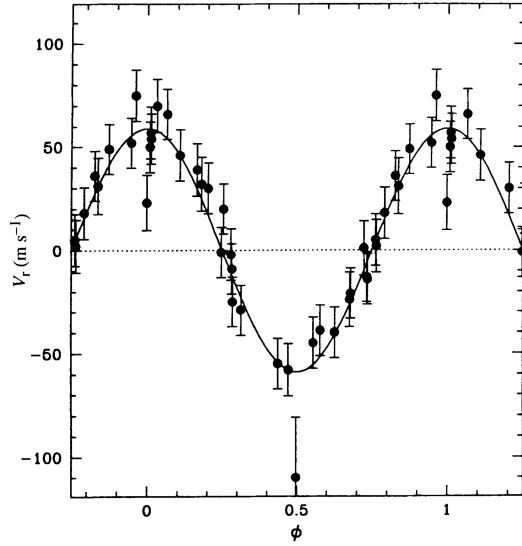


Figure 2.4: Example phase-plot of the radial velocity of a planet-star system (a hot Jupiter orbiting a Sun-like star) orbiting their common barycenter. From Mayor and Queloz [1995].

2.2.3 Transit photometry

The most successful technique of detecting exoplanets (in terms of the sheer number of exoplanets detected) so far, is the transit photometry. The technique involves careful monitoring of the flux of a star over time: when a planet pass in front of it, a decrease in flux will be observable (see Figure 2.5) – if the observation equipment is sensitive enough, or the planet is large enough to cover a significant portion of the host star. Measuring the transit allows for the orbital period and the relative radius of the planet to be determined. The following equation is used to describe the relative radius of the planet.

$$d = \left(\frac{R_p}{R_\star} \right)^2, \quad (2.1)$$

with d being the transit depth, R_p being the radius of the transiting exoplanet, and R_\star being the stellar radius.

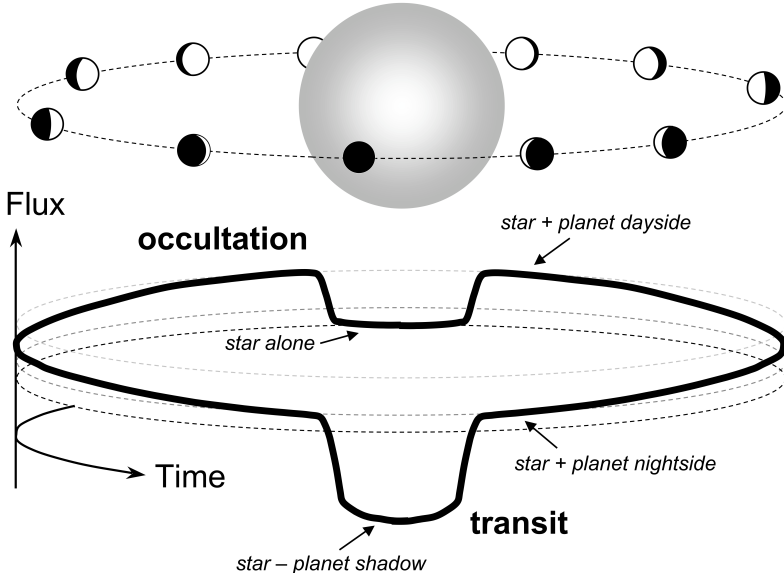


Figure 2.5: Illustration of different orbital phases of an exoplanet around a star. From Winn [2010].

Determining the orbital period requires measuring at least two transits, but in common practice several transits are necessary. At the occultation of the planet, the stellar flux can be determined without contamination from reflected light of the planet. In between these points, the relative flux will change due to light reflected off of the exoplanet (top part of Figure 2.5) and measuring this phase curve can yield the planetary reflectance.

This technique is best suited for large planets, close to their host star (so their orbital period is short) and with stars not excessively luminous, but it is, in fact, also the best method for small planets. Small planets will not affect the barycenter of their system much and thus not have great effects on the RV-signal of their host star. Also, smaller planets are difficult to detect with direct imaging as they will reflect less light than larger planets.

While the method is relatively simple and can yield an impressive amount of information (for a comprehensive guide on transiting exoplanets, see e.g. Winn [2010]), one can only learn so much about the exoplanets if only observing in one pass-band.

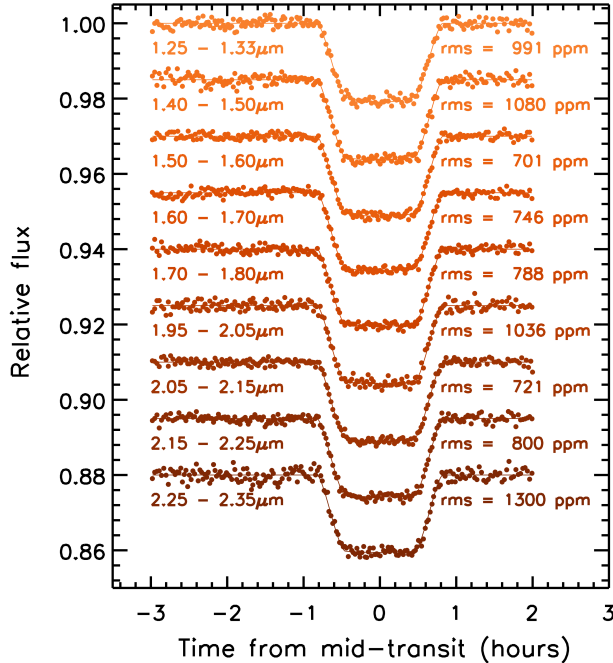


Figure 2.6: Varying transit depths of WASP-19b. Adapted from Bean et al. [2013].

If the transit is observed in several spectral bands (e.g. using filters), the radius of the planet will seem to change – for an example in the NIR, see Fig. 2.6 – this is due to the atmosphere of the planet. This method of observing the varying radius is effectively very-low-resolution spectroscopy, limited by the number of pass-bands and their widths used. Increasing the spectral resolution means going from very-low-resolution spectroscopy to another field, known as spectrophotometry. Even further beyond lies the “regular” high-resolution spectroscopy.

2.2.4 Spectrophotometry

To analyse the exoplanetary atmospheres, a wide spectral coverage is needed as the constituents of the atmospheres might not all have spectral features in a single pass-band. The method is generally known as spectrophotometry and in the case of exoplanet observations, it combines transit photometry with spectroscopy in and out of transits (see Figure 2.5). Transit spectroscopy is the most successful method of studying exoplanetary atmospheres so far (see e.g. Madhusudhan [2019] and the references therein) – mainly due to the large number of planets

found by the transit method and their optimal geometrical configuration for easier observations of potential atmospheres. A particular case of spectrophotometry – transit spectroscopy – is of great interest, as the technique can be used to probe the atmospheres for broad-band features as well as individual spectral lines. In this method, the “transit spectrum” is observed and subsequently analysed. The transmission spectrum is essentially the difference between the in-transit and the out-of-transit spectra, normalized by the out-of-transit spectrum. Three examples of transmission spectra can be seen on Figure 2.7.

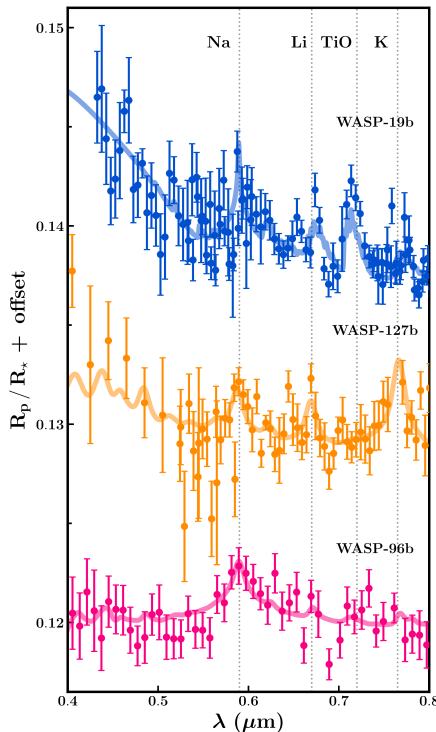


Figure 2.7: Transmission spectrum of three different exoplanets, with an offset for clarity. The y-axis shows the transit depth, see eq. 2.1. From Madhusudhan [2019].

Obtaining a transmission spectrum is possible during the primary eclipse, as the spectral features of the exoplanetary atmosphere are imprinted on the stellar spectrum. The physical reason why imprinted spectrum is present is that the stellar light passes through the atmosphere of the exoplanet at the day/night-terminator – near the edge of the planetary disc, from the observer’s viewpoint. This is conceptually quite similar

to the images of the atmospheres of Solar system objects imaged by probes such as Cassini and New Horizons (see Figure 2.8). The planet covers part of the stellar disc and this imprint of the exoplanet and its atmosphere is etched into the stellar spectrum.



Figure 2.8: The hazy atmosphere of Pluto, as seen by the New Horizons probe in 2015. Credit: NASA/JHUAPL/SwRI

By measuring the transit depth of the exoplanet eclipsing the star, in different wavelength bands, the atmospheric height can be probed, which is relevant for measuring the extent of the atmosphere. If the spectral resolution (defined later, in Chap. 4) is increased, identifying specific spectral features – like water, sodium, etc. – is possible. Ground-based facilities can only observe in the wavelengths not obscured by the Earth's atmosphere, so in order to further the current understanding of exoplanetary atmospheres, the observations will have to be conducted from space.

Satellites 3

From the previous chapter, it should be clear that in order to effectively study the atmospheres of exoplanets in spectral bands from UV to IR, the observations will have to be made from space. This calls for satellite observatories. Several different types of satellite-based missions for observing exoplanets (and space-phenomena in general) exists. Some of the most important ones (at least for exoplanetary science) are the Hubble Space Telescope (HST)¹, the Transiting Exoplanet Survey Satellite (TESS)², and the Kepler mission³.

Currently, the only large space-based platform with a broad spectral coverage is HST [Madhusudhan, 2019], that can observe from UV to NIR. Other missions, such as the Spitzer space telescope⁴, only observed in the IR, while TESS and Kepler both observe in the visual to NIR (see Ricker et al. [2014] and Koch et al. [2010]). Given the age and current mission outlooks for the HST, there will be no single telescope to cover broadband spectroscopy from UV to IR, at least not until the Large Ultraviolet Optical Infrared Surveyor (LUVOIR) mission (Kouveliotou et al. [2014]) or the Habitable Exoplanet Imaging mission (HabEx) (Gaudi et al. [2019]) start in the 2030s. The James Webb Space Telescope will, when it is operational, cover wavelengths from 0.6 μm in the visible, to 30 μm in the mid-infrared (see e.g. Gardner et al. [2006]).

Given the mission cost and restrictions on observation time on such missions, it might be more feasible to explore the possibilities of smaller satellites. An example of this is the nanosatellites and a subset of those are the CubeSats – revered for their great versatility and low cost. Already, more than 1300 CubeSat have been launched⁵ as of October 2020.

¹https://www.nasa.gov/mission_pages/hubble

²<https://tess.mit.edu/>

³https://www.nasa.gov/mission_pages/kepler

⁴<http://www.spitzer.caltech.edu/>

⁵According to <https://www.nanosats.eu/>.

The main advantage of these modular satellites is the option of using off-the-shelf components, such as On-Board Computers, power systems and spacecraft Attitude Determination and Control System (ADCS). This enables such a mission to be ready for launch extremely quickly compared to larger missions. There are many interesting CubeSat missions, but on the topic of broadband observations, there is not. However, the proposed CUBESPEC mission (as described in Raskin et al. [2018]) could fill this position as a small-platform observatory for a wide spectral coverage.

3.1 Space environment

In this section, the effects of space environment on satellites will be further explored: Trapped radiation belts, effects of atmospheric drag, and cosmic rays will all be described. The various effects will be very dependent on the actual orbit of the potential satellite. For a low-Earth orbit (LEO) satellite, atmospheric drag might present the most dominant effect, while for other types of orbits (Sun-synchronous orbit, Molniya orbit, etc.) the extensive radiation from the Van Allen belts and cosmic rays might be more dominant. These ramifications will affect a future mission, and can severely limit the data quality of spectroscopic measurements.

3.1.1 Trapped radiation belts

Surrounding the Earth are belts of trapped electrons and ions (mostly protons), being held in place by the Earth's magnetic field (van Allen and Frank [1959]). The two belts are toroidally shaped regions – the stabler inner belt has the highest concentration of electrons, while the outer has more protons.

When describing the location of the belts, the L-shell value is of great use: It is a surface created by rotating a magnetic field line around the magnetic dipole axis. The L-value of the dipole magnetic shell is thus its equatorial radius, measured in Earth radii. The surface is described by:

$$R = L \cos^2 \lambda \tag{3.1}$$

with R being the distance from the point dipole in the Earth's centre, measured in Earth radii, and λ being the magnetic latitude. For the original and extensive introduction to L-shells, see McIlwain [1961].

Using the L-shell values, the inner radiation belt is located between $L \sim 1.2$ and $3 R_\oplus$, while the outer is located between 3.8 and $7 R_\oplus$ (Ganushkina et al. [2011]). This means that a large part of satellites in LEO will spend some amount of time in these areas – potentially leading to damage to electrical subsystems.

Detectors, solar arrays, and microelectronic devices will all be degraded by extensive exposure to the highly energetic particles located in the Van Allen belts, leading to a shorter mission time-span. Photo-detectors onboard satellites can also be affected by these streams of high-energy particles (and other energetic particles in general), as described in the following section.

3.1.2 Energetic particles

There are several different types of high-energy particles that can affect satellites, their detectors, and their microprocessors on-board. While the trapped radiation belt is the most common source of energetic particles for LEO satellites, cosmic rays are another type of high energy particles that affect satellites in all orbits. Cosmic rays are mostly protons (Schneider [2006]), that usually originate from supernovae (see e.g. Ackermann et al. [2013]) and other sources outside of the Solar system. Another type of highly energetic particles arriving at Earth is produced in the Sun. They are often detected following solar flares and coronal mass ejections (Reames [2013]). The highly energetic particles are a problem for electric subsystems of a satellite, as they can lead to degradation of the electronic components through atomic displacement and ionization. In a detector made of silicon, atomic displacement can result in severely degraded efficiency in the affected area or even entirely dead pixels. The cosmic rays can also result in bits flipping, potentially resulting in a multitude of failures, among other effects. For a more complete dissertation on the effects of high-energy particles on electric systems, see Leppälä et al. [1989].

3.1.3 Effects from the atmosphere

For satellites in LEO, or with perigees in that orbital height, the atmosphere will shorten orbital and mission lifetime, mainly due aerodynamic drag. The aerodynamic effects on a spacecraft are minuscule in the extremely rarefied atmosphere of LEO. However, the effects are still present and will over long time-periods lead to a significant reduction in orbital velocity – leading to the eventual de-orbit of the satellite.

The drag will remove energy from the orbit, resulting in a lower orbit with even higher atmospheric density, resulting in an ever-increasing drag with an exponential growth. Over time, the orbit height will have decreased so much that the satellite reenters the atmosphere and burns up or crashes down – depending on the size.

The equation describing the atmospheric drag is (see Larson and Wertz [1992]):

$$a_D = -\frac{1}{2}\rho \frac{C_D A}{m} V^2 \quad (3.2)$$

with a_D being the acceleration due to the atmosphere, ρ is the atmospheric density, C_D is the coefficient of drag (often ≈ 2.2 , Mehta et al. [2014]), A is the cross-sectional area, m is the satellite mass, and V is the velocity of the satellite relative to the atmosphere. The *Ballistic Coefficient*, BC is defined as $BC \equiv m/(C_D A)$.

From this equation, the lifetime of a satellite in a circular orbit can be found as:

$$L \approx -H/\Delta a_{rev}, \quad (3.3)$$

where $\Delta a_{rev} = -2\pi BC\rho a^2$, and H being the atmospheric scale height. From Larson and Wertz [1992].

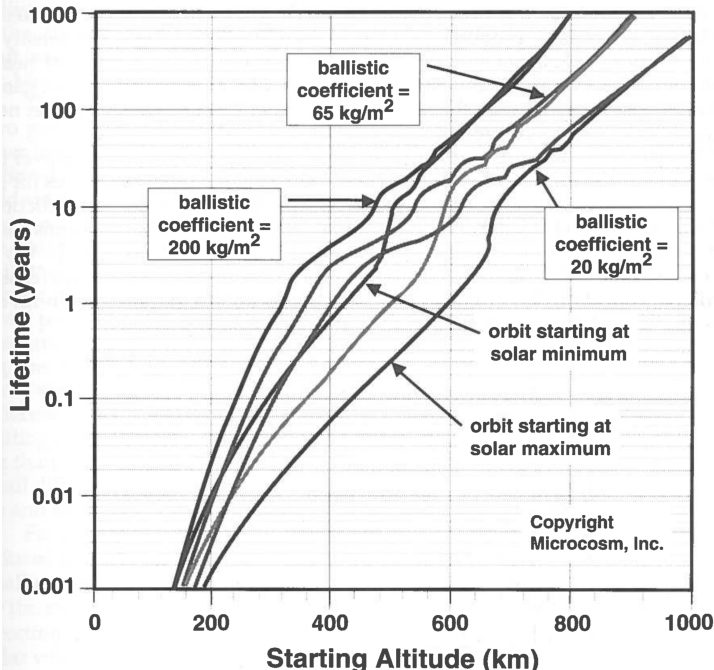


Figure 3.1: Orbital lifetime, during Solar minimum and maximum, for three different Ballistic Coefficients. From Larson and Wertz [1992].

Given that the atmospheric scale height increases during solar maxima, the lifetime of missions in LEO launched during such a maximum are notably shorter than those launched during solar minima, which can be seen on Figure 3.1.

All of the above-mentioned environmental effects can affect the spacecraft substantially and will thereby decrease the mission lifetime. Therefore, it is important to consider these environmental parameters when designing a space-based mission.

3.2 ADCS, spacecraft jitter

When the satellite reaches its designated orbit and starts observing stars, slight vibrations and motions will make the star move around on the detector plane. This attitude noise can arise from many different sources, some of which are shown in Table 3.1. This effect will lead to severely changed spectroscopic measurements, as the jitter will shift light away from the optical path of the system. This will be introduced in Chapter 4. For now, the focus of this section is the cause and how to mitigate the effect.

Pointing error type	Potential source(s)
Environmental disturbances	Solar pressure noise
Drive mechanisms	Solar array, instruments, antenna
Actuator intrinsic error sources	RW imbalances, thruster noise
Sensor bias and noise	Star tracker, gyroscopes, GPS
System dynamics induced errors	Fuel sloshing

Table 3.1: Different sources of time-random pointing error sources. From ESA [2011]; Pointing error engineering handbook.

The effects of this random motion seen on the detector as changes in pitch, yaw and rotation, can be mitigated by having a good ADCS. Commonly used attitude determination systems include star trackers and gyroscopes, and attitude controllers are often reaction wheels (RW), magnetorquers, or small thrusters.

To describe spacecraft attitude (essentially the pointing direction) and the potential short timescale noise introduced by vibrations, an approximation is utilised:

$$x(t + dt) = x(t) + dx(t, dt) - \alpha \cdot (x(t - \Delta t)). \quad (3.4)$$

Here, x is the position of the star on the detector (either yaw or pitch), α is the gain of the attitude control system, and Δt is the time delay of the determination of the position.

Effectively the target will move around but always be corrected towards the designated zero-point so the spread ideally never becomes too large. Having a too large gain results in over-correcting the random movement, which can often be worse than doing nothing, and having too little is not helpful either. For the time delay, there are also a few restrictions: If the time delay is set to be very large, the system will not correct often enough, resulting in a slowly deviating position. Ideally, the system corrects every infinitesimally small time step, but in reality, this is limited by the processing of the measured attitude and performing the correcting maneuver.

While the effect of jitter might not be immediately apparent, this ramification will be a major part and limiting factor in the simulator introduced later.

Spectroscopy & Optics 4

By now, it should be clear that the observations of exoplanetary atmospheres will (at least in large part) have to be done from space in order to get the full spectral coverage that is desirable. The method of obtaining knowledge is through spectrophotometry, but the method of acquiring the spectra is not yet clear. In this chapter, the concept of spectroscopy is introduced. Different methods of obtaining stellar spectra are also established, as well as some of the scientific parameters unlocked by them.

In general, spectroscopy refers to the study of spectra – in the case at hand, it refers to the study of spectra of stars. Such a spectrum has an abundance of spectral absorption lines from different atoms and molecules, that absorb part of the outgoing light from the star, due to electrons transitioning between energy levels due to photon absorption. By studying the position, movement, depth, and width of the spectral lines, several different parameters of the object can be determined. The movement of the spectral lines, for example, could be due to the star orbiting the common barycenter of the system – as seen in multiple star systems or in planet-star systems. Other parameters can likewise be found by careful study of the spectral features.

4.1 Spectrometers

A spectrometer – or more commonly in astronomy, a spectrograph – is one of the most common instruments used to obtain spectra. The principle was first explored by Joseph Von Fraunhofer, who invented the spectroscope and subsequently (re)discovered¹ the absorption lines present in the Solar spectrum (Brand [1995]). Since he invented the spectroscope, the instrument has been used extensively in astronomy, chemistry, and physics, among many fields.

¹The lines were first described by the English chemist William H. Wollaston, see Wollaston [1802].

Briefly put, three basic components are always present in spectrographs: a slit, a dispersive element, and a detector of some sort. The slit is used to eliminate light from sources other than that of the object of interest, but also to set the spectral resolution. The dispersive element will spread the incoming light from the slit into its respective colours – simple spectrographs might use prisms of glass, but modern ones often use echelle gratings, such as ESPRESSO (e.g. Pepe et al. [2020]), for higher spectral resolution.

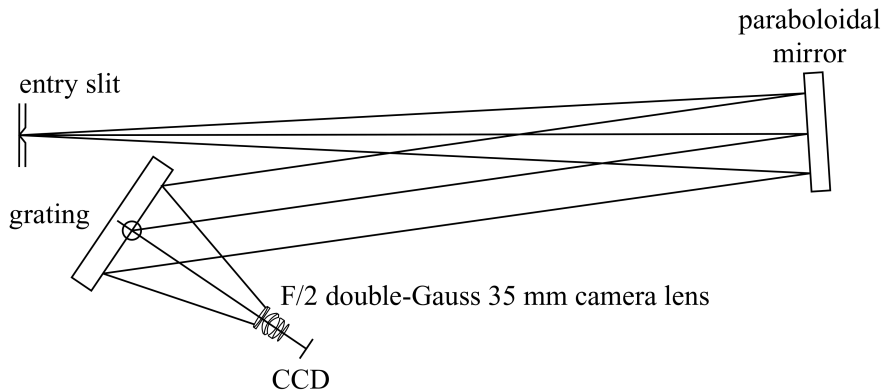


Figure 4.1: A simple schematic view of a spectrograph. Most modern spectrographs are built using similar setups. From James [2007].

When considering a spectrograph, it can be beneficial to evaluate its resolution power, R , defined as

$$R = \frac{\lambda}{\Delta\lambda}, \quad (4.1)$$

with λ being the wavelength and $\Delta\lambda$ being the smallest difference in wavelength resolvable by the setup. A more narrow slit leads to a smaller imprint on the detector and it also affects the spectral resolution – a wider slit means lower resolution. The advantage of a narrow slit is thus a higher spectral resolution and less susceptibility to the effects of spacecraft jitter. The latter benefit is an effect of the PSF edges not making it past the slit mask, where the jitter is most pronounced (as seen on Figure 4.2). If the slit is wide, the movement of the PSF is seen, and thus there will be a larger variation of the final exposure if the jitter and slit are comparable in angular extent. A wider slit, however, has the advantage of an increased amount of photo-electrons arriving at the detector, meaning shorter exposure times. But a wider

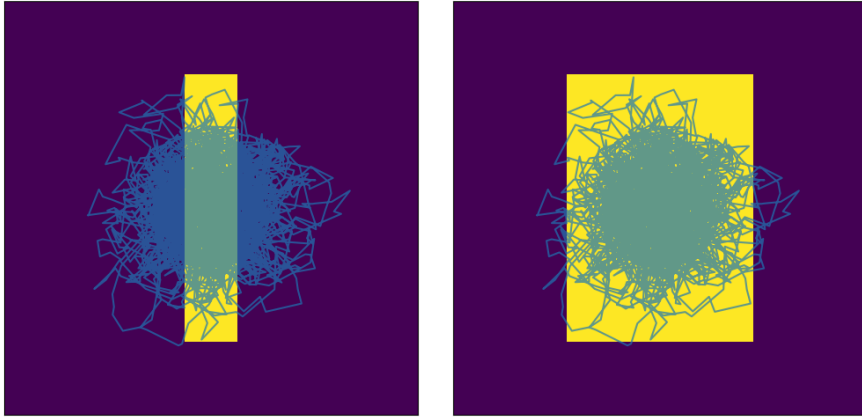


Figure 4.2: Comparison of a narrow and a wide slit, with spacecraft jitter imposed on top. The setup with a narrow slit will be less affected, as the target will be within the slit during the majority of the exposure.

slit also has lower spectral resolution and is potentially more affected by jitter, if the ADCS is poorly constrained. In general, the spectrograph has to be made with all of these considerations in mind. The final setup depends heavily on the intent of the setup – for high-resolution spectroscopy, a narrow slit might be desirable, but then the collecting area of the telescope has to be larger or exposures longer. For lower resolution spectroscopy a wide slit might be desirable, as the telescope can be considerably smaller, which makes for cheaper missions, a more compact payload design, etc.

4.2 Graded Prisms – Grisms

Instead of using a grated mirror or similar, as seen in Figure 4.1, an alternative method can be utilised: The graded prism – also known as a *grism*. Combining the elements of the dispersing prism and grating, the resulting spectrograph can be made extremely compact. The grism can simply be placed just before the detector plane so that the already collimated light will be dispersed into a spectrum onto the photo-detector. A clear effect of placing this filter-like mask over the detector plane without any slit, fiber or similar is that all the objects in the field-of-view will be dispersed. This can result in spectra overlapping on the resulting image, as seen on Figure 4.3. Should two spectra overlap, it can be hard to deconvolve them. The technique is, therefore, naturally limited to

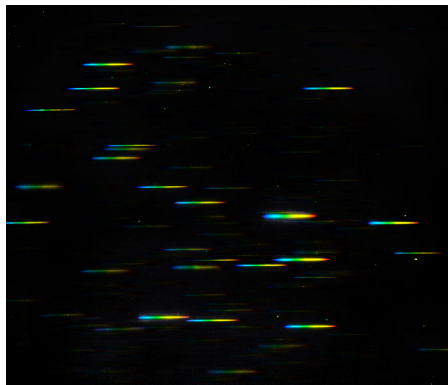


Figure 4.3: Illustration of a grism image, representing data coming from NASA/ESA HST’s WFC3 in grism spectroscopy mode.

fields-of-view with few objects of interest. The main advantage of the grism technique is versatility. The entire setup can be changed quickly from regular imaging to spectroscopic imaging – the filter wheel can simply be shifted the slot containing the grism. However, the main disadvantage is the considerably lower spectral resolution, often in the order of $R \lesssim 2000$ (e.g. NIRCam on the upcoming JWST, see e.g. Greene et al. [2016]).

4.3 Hyperspectral imaging

A relatively novel instrument, and one not used extensively in astronomy yet, is hyperspectral imaging cameras. Used mostly for Earth observations by satellites, such as the GOMX-4B satellite (see e.g. Alminde et al. [2017] and Esposito and Zuccaro Marchi [2019]), ESAs Sentinel-5P (see e.g Kleipool et al. [2018]), or the upcoming Sentinel-10 CHIME (see Nieke and Rast [2018] and the references therein). Hyperspectral data has been used to monitor vegetation fluorescence, atmospheric changes, water resources, natural disasters, urban areas, and meteorology (see e.g Strese and Maresi [2019]). The apparent uses of hyperspectral data for Earth observations are obvious, but the potential use in astronomy is also substantial. A hyperspectral instrument could be a cost-effective alternative to a low-resolution spectrograph in space, an otherwise expensive and very delicate instrument, vulnerable to misalignments of the optical components. A hyperspectral imaging unit could function as a compact and cheaper alternative.

4.4 Point Spread Function

Stars are so far away that they have no angular extension but appear as point sources (except for a select few examples). Through a piece of optics (telescopes, eyes, etc.), however, the stars will appear as broadened out discs. To describe this “transformation” from point to larger disc, the Point Spread Function (PSF) is used. The spread is dependent on wavelength, as optics will refract the light differently depending on the wavelength.

The reason why point sources are broadened out is due to the physical principle of diffraction and interference. It can be explained with the following: A wavefront of light is travelling toward a circular aperture or a slit. As the light propagates through the slit, the light gets diffracted – as explained by the Huygens-Fresnel principle, stating that a wavefront of light can be thought of as many smaller spherical wavelets (e.g. [Pedrotti et al., 2017, p. 32]). All of these wavelets will continue to propagate forward, where the intensity is measured. The setup can be seen on figure 4.4.

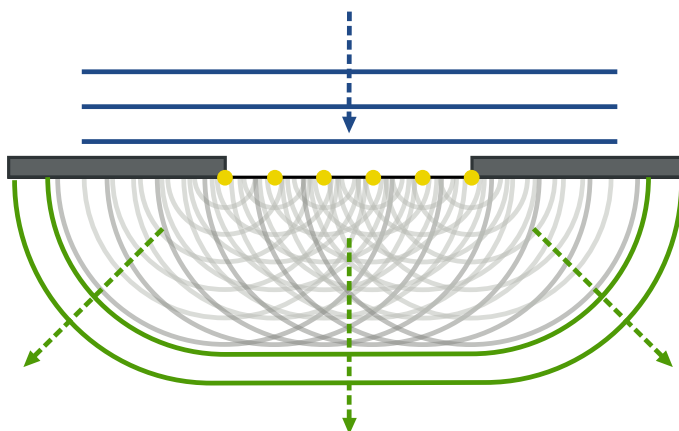


Figure 4.4: Single aperture diffraction, also generally known as Fraunhofer diffraction. The blue lines represent an incoming wavefront, the yellow dots are wavelets propagating through the slit. The green lines are the new resulting wavefront. By norro, CC BY-SA 3.0, <https://commons.wikimedia.org/w/index.php?curid=1944668>

At the measuring plane some distance away from the slit, a pattern will arise. This is due to constructive and destructive interference of the light. If the wavefronts of two wavelets arrive at the measuring plane in phase, they will constructively interfere and if they arrive out of phase they will destructively interfere.

The central part, directly in front of the slit will be most illuminated, followed by an annulus of darkness, again followed by light, and so on. The pattern was first described in detail by George Airy (Airy [1835]) and are named after him. An example of an Airy disc can be seen on Figure 4.5.

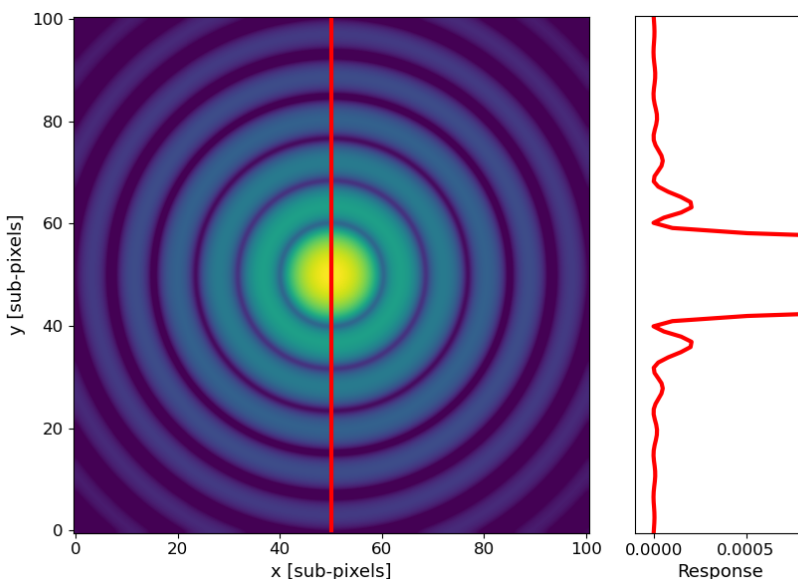


Figure 4.5: The resultant Airy diffraction pattern from a circular aperture. Similar patterns will be visible in telescopes. The contrast has been enhanced for clarity.

An optical system, such as a telescope, is said to be *diffraction-limited* if it is capable of resolving the PSF, and no deviations from it are present. For the sake of simplicity, the PSF is often approximated as Gaussian to alleviate computation time, etc. This 2D-Gaussian distribution is highly dependent on the optical system. Changing the focus of the optical system will naturally change the PSF as well – a more defocused system result in larger PSFs and this might prove beneficial depending on the end goal.

Materials, such as gasses, between the detector and the observed object can lead to severe distortions of the PSF. The main contributor for many systems is the Earth's atmosphere – but since the case at hand is a satellite-mission, this effect is largely negligible. For a view of how the PSF of the future JWST will look, see Fig. 4.6.

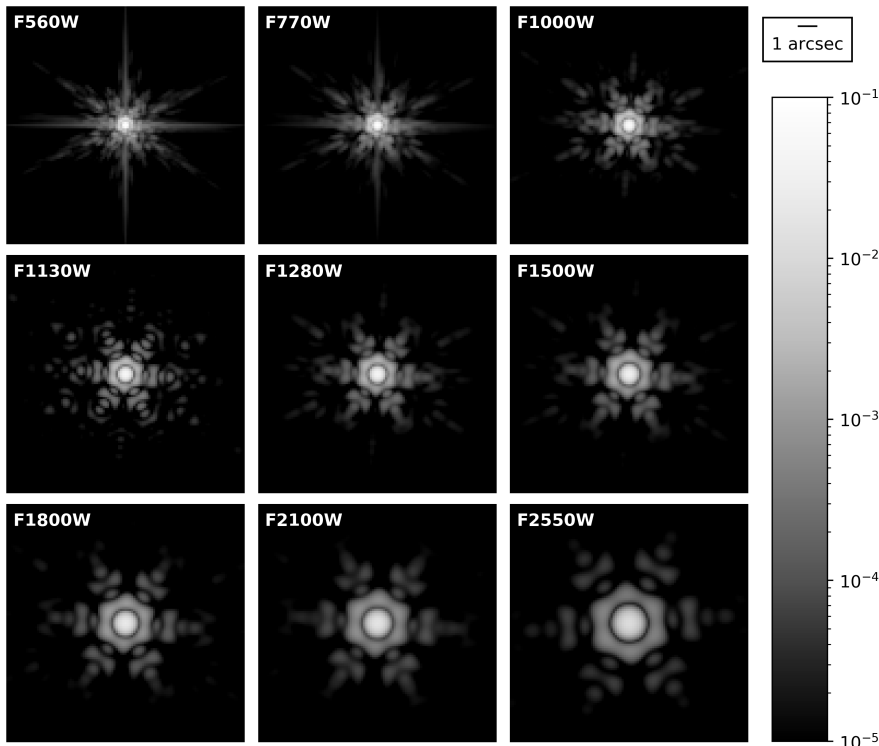


Figure 4.6: Simulated PSFs of the Mid-Infrared Instrument on the JWST.
From [https://jwst-docs.stsci.edu/mid-infrared-instrument/
miri-predicted-performance/miri-point-spread-functions](https://jwst-docs.stsci.edu/mid-infrared-instrument/miri-predicted-performance/miri-point-spread-functions)

Theory of Charge-Coupled Devices 5

To determine if detection of an exoplanetary atmosphere is possible with a given setup of telescope onboard a satellite, the photo-detector used has to be understood in great detail. That is the purpose of the following chapter.

Since the invention of the telescope, astronomers have been observing the heavens with greater precision than ever. Yet, the astronomers of old had to draw and describe what they saw – there was a need to quantify their observations. Enter the charge-coupled device (CCD). It is a type of photo-detector made using silicon, a semiconducting material. The device was invented in the late 1960s (e.g. Janesick and Blouke [1987]) and have since then been used extensively in both astronomy and everyday appliances such as digital cameras and copy machines, to name a few. Despite only having been used for the last ~ 40 years, almost every professional observatory, as well as many amateur telescopes use CCDs as their primary astronomical detector. The main reasons are the extremely low noise, high quantum efficiency in the visible spectral band-pass, and their relative ease of use. All of these aspects will be covered in the following section.

5.1 CCD operation

An oft-used analogy for the operation of CCDs is that of the field covered with buckets on conveyor belts. Imagine a field filled with buckets in a grid for collecting raindrops. The raindrops represent photons, and the buckets represent pixels. After a rainstorm (representing the CCD exposure time) the amount of water in each bucket is measured. This is done by moving the buckets on conveyor belts in an orderly fashion. Every row is moved to the rightmost column which is moved one bucket at a time to the metering station (see Fig. 5.1). In reality, the mechanism used to generate an electric signal from incoming photons is

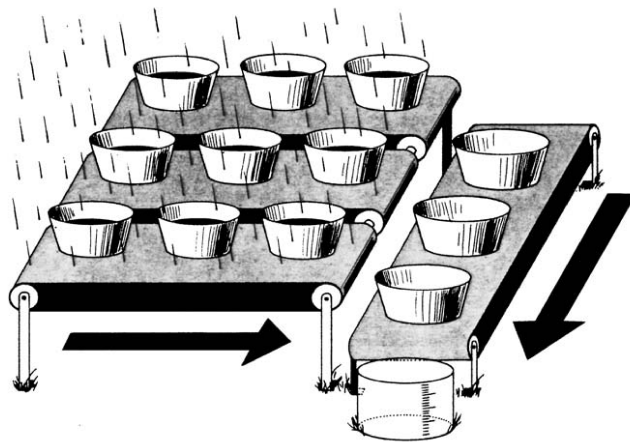


Figure 5.1: Graphical depiction of the field-with-buckets-analogy described above. At the metering station, the amount of rain (photoelectrons) is measured. From Janesick and Blouke [1987].

the *photoelectric effect*: If a photon within the correct wavelength band (i.e. energy) strikes the silicon, it will be absorbed. For this reason, the terms *electrons* and *photons* will be used more or less interchangeably in the context of CCDs and their measurements. The effective range of detectable energies of incoming photons span from 1.1 eV to 4 eV (e.g. Howell [2006]). This means that a CCD will effectively appear transparent to photons with higher or lower energies. Because of the absorption of a photon, an electron will be moved from the valence band to the conduction band, where it will be held in place by sub-pixel structures, called gates, until the read-out occurs. By *clocking* the gates in turn, all the electrons in each pixel can be counted – that is if there is no loss of electrons along the way to the register. The efficiency of these transfers is called the charge transfer efficiency (CTE) and will be explained in Section 5.4.

5.2 Flat field, dark current & bias

Images captured with CCDs are close to being noise-free, but several things work against capturing perfect images. There are ways of correcting for some of these imperfections and they will be discussed in the following subsections. The section is meant as a general introduction to the field of CCDs, and the aspect are in large part not further considered.

5.2.1 Flat field

A flat field is essentially just an image that you subtract from all your observations in order to remove errors and background noise. Flat fielding is a necessary part of observations due to the inherent differences in individual pixels - in theory, every pixel should be identical, but minuscule differences make their quantum efficiency (QE), CTE, etc. slightly nonuniform. This can be mitigated by constructing a flat field image to improve the final data image. A flat field can be constructed by illuminating every pixel with the same amount of light - a "flat" illumination - for some time. This is usually done several times and the averaged of the flat fields, the "master flat field" is used. In theory, it is simple, but in reality, obtaining the flats is tricky. Finding a spectrally and spatially flat area to image is not trivial: Often the twilit sky or a patch inside the telescope dome is imaged over several short exposures.

5.2.2 Dark current

Dark current is the thermal noise of the CCD. When the temperature of the CCD is high enough, one will start to see some extra signal. This comes from electrons being freed to the conduction band by thermal excitation alone and they will be indistinguishable from the captured photo-electrons. As the name suggests, thermal excitation is heavily dependent on temperature, which is why cooling the CCD is often used to minimize this noise. For this project, which focuses on observations from space, thermal noise will not be a limiting factor and is therefore not included.

5.2.3 Bias

Bias images are used to measure the noise of the CCD with zero exposure time. Upon read-out, zero collected photo-electrons will translate to a mean value around zero ADUs. To avoid the negative readings, CCDs are fabricated to have an offset of the mean value (typical values are 400 ADUs per pixel, Howell [2006]). The exact bias level can be found by reading out a CCD after an exposure of 0 seconds. This is thus a detection of all on-chip electronic noise, A/D converter noise, etc., and it can be used to correct for these effects in the final image.

5.3 CCD gain & non-linearity

The gain of a CCD refers to the relation between electrons needed to create one Analogue-to-Digital Unit (ADU). It is described as electrons per ADU:

$$g = \frac{e^-}{\text{ADU}}. \quad (5.1)$$

Values can range from simple photon counting ($g = 1$) up to a gain of 150 or more and are specific for individual CCDs. The relation between electrons and ADUs follow a linear trend but can become non-linear for large input values of electrons.

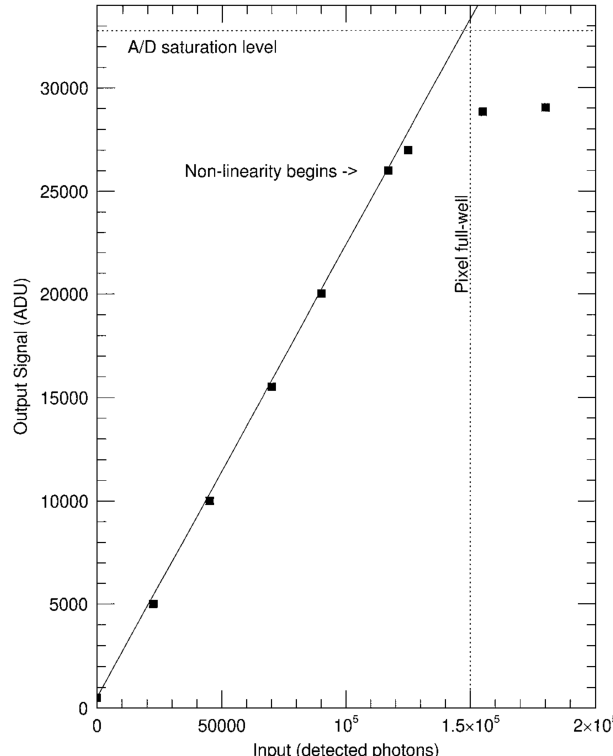


Figure 5.2: Linearity curve for a generic CCD. At 1.17×10^5 photons, the output ADU starts to deviate from the previous linear trend. From Howell [2006].

There are two types of non-linearity: Differential non-linearity and integral non-linearity, the latter being of most importance. Differential non-linearity arises from the fact that the analogue-to-digital converter

works in steps of whole ADUs. Fractional counts up to $0.49\bar{9}$ will be counted as zero and values above will count as 1. This type of non-linearity noise is also called digitization noise. Integral non-linearity is the total non-linearity produced by the A/D converter. For the purposes of this thesis, non-linearity will not be treated any further, as it is rarely the limiting factor in CCD usage.

5.4 Charge Transfer Efficiency

charge transfer efficiency (CTE) is how well the electrons are moved without loss during the read-out process. It is a fraction of the total excited electrons, as some of them inevitably will be lost. Values for good CCDs are approaching 0.999 995 (Howell [2006]), so quite close to fully efficient (i.e. a CTE of 1). In everyday use of a CCD, the degradation of CTE will not be all that cumbersome, but if placed in harsh environments or exposed to high-energy photons, the CCD structure will be damaged and the CTE will start to decrease noticeably. This will become visible as streaks in the image, as seen on Figure 5.3.

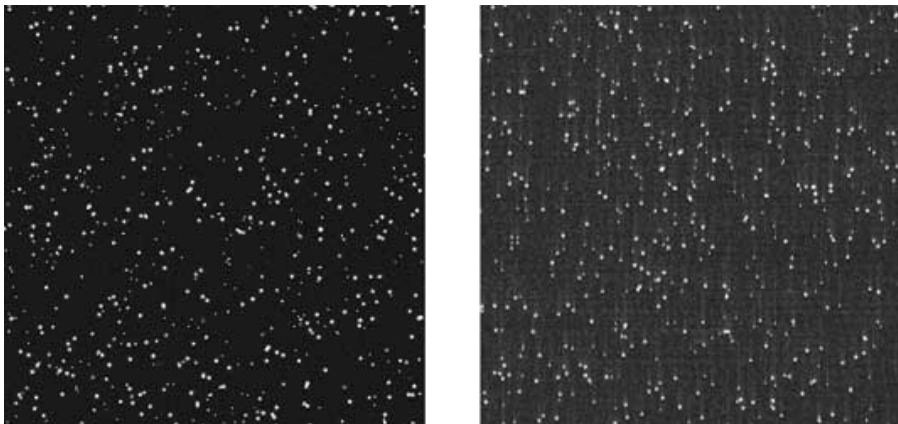


Figure 5.3: An example of good and bad CTE. Notice how the visible streaks on the right image are slightly more intense further from the bottom, where the A/D converter is. From <https://wfc3.gsfc.nasa.gov/MARCONI/cte.html>

5.5 Sub-pixel structure

CCD pixels are very sensitive to incoming photons, but their sensitivity to the light varies over each pixel. In fact, the sensitivity is also dependent on where on each pixel the photon strikes. This means that the number of photo-electrons being generated can vary on each pixel. The variation in sensitivity can be due to fabrication defects or photons striking in areas with wiring, gates, etc. The effect of sub-pixel-level sensitivity will be included in the simulator, which is described in Chapter 6.

5.6 CMOS detectors

A complementary metal–oxide–semiconductor (CMOS) sensor is another type of photodetector. It also absorbs incoming photons due to the photoelectric effect, as with CCDs, but the read-out process is inherently different from that of the CCDs. Instead of moving the charges to the read-out column by clocking the gates in the pixels, the photo-electrons are converted to voltage directly on each pixel. Every column is then moved to an A/D converter at the bottom of each column. This process will drastically increase the read-out time, as there are many more A/D converters than with a CCD. An obvious disadvantage is that the increased amount of A/D converters results in a less homogeneous read-out process - the individual converters might have slight imperfections and this means more time spent correcting for this effect. Also, the full well capacity (FWC), which is the maximum amount of charge capable of being stored in each pixel, is considerably lower in CMOS sensors due to amount of on-pixel electronics (A/D converter and wiring) taking up more space than for a CCD with relatively simple gate structures.

These are just some of the reasons why CMOS sensors are not widely employed in astronomy, despite being cheaper than CCDs and more generally used by the masses. However, there have been made several improvements in the last few years alone, so it would not be surprising if the CMOS field took the CCDs place as the optimal detector in the future.

Simulator 6

With all of the relevant background knowledge covered, the main focus of this thesis can begin. The majority of the work process has revolved around creating a script capable of simulating 2D spectra from low-resolution spectrographs. This was done in order to properly determine if a given setup would be able to detect exoplanetary atmospheres and this is where computer-simulations come into play. The main workload of this thesis was thus to make and test such a simulator. This will be described and explained in this chapter.

The simulator itself is a conglomerate of many smaller functions (modules) and is showed conceptually in the flowchart in Figure 6.1.

Before explaining the entire simulator, a list of all the input parameters will be presented – along with their corresponding formats and units. This is to give potential users a robust insight into how the different aspects of the simulator work.

Following this, the individual modules of the simulator will be explained in more detail, starting in Section 6.2. The explanation is divided into three “phases”, where each step is further elaborated upon. At the end of the chapter, a list of auxiliary function will be presented. These functions are meant to be useful tools for the user and they are capable of generating many of the inputs essential for the simulation.

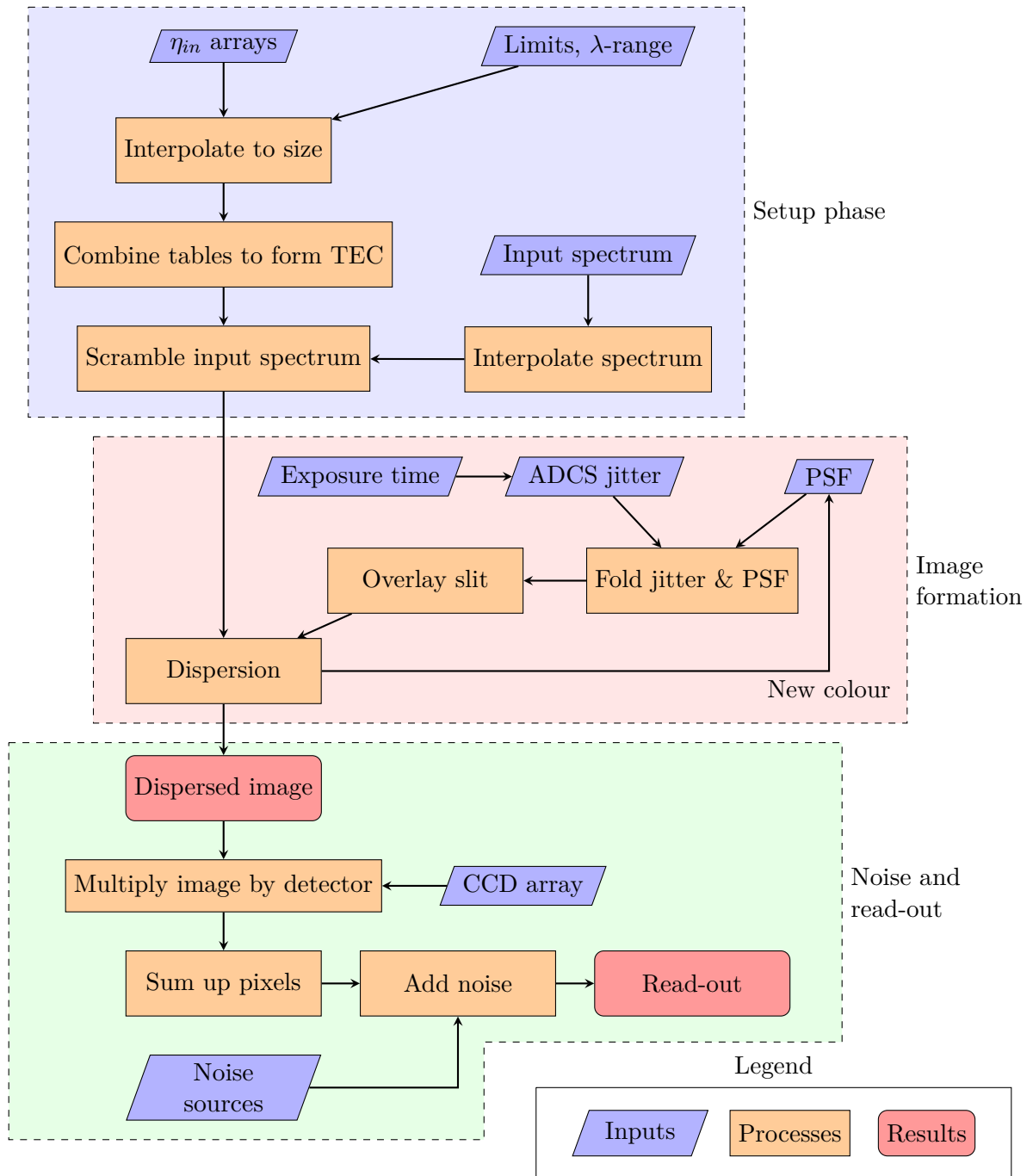


Figure 6.1: Flowchart of the simulation process.

6.1 Input format and units

For the simulator to work, the inputs must have the correct format and units. This section outlines the input parameters and they will be described using the following template:

variable name*Description of input*

Format, with a brief explanation

[*Units of inputs*]

Notes: Further information about the input

First, the strictly necessary inputs are listed, followed by the optional inputs. The latter can automatically be generated by the simulator, albeit in simplistic ways, if not supplied by the user. It should be stated, that the generated inputs are by no means fully realistic models and to simulate such would be beyond the scope of this project.

It might be desirable for the user to be able to specify individual parameters, so many of the inputs are kept optional.

6.1.1 Necessary inputs

in_spec*Input science spectrum*

2D array, 2 columns. The first column contains the wavelength, the second contains the photon counts.

[nm], [counts $s^{-1} nm^{-1} cm^{-2}$]

Notes: If the wavelength coverage is incomplete, i.e. does not cover to the specified wavelength span, values will be extrapolated.

col_area*Effective collecting area of the telescope*

Float, single value.

[cm^2]

Notes:

img_size*Size of the CCD*

Tuple, 2 integers.

[pixel], [pixel]

Notes: The size of the final image. Some of the optional inputs must be of the same dimensions like this.

pl_scale

Plate-scale of the detector

Float, single value.

[arcsec mm^{-1}]

Notes:

pix_size

Pixel size of the detector

Float, single value.

[mm pixel^{-1}]

Notes: the physical size of each pixel of the detector.

bg_spec

Background spectrum

2D array, 2 columns. The first column contains the wavelength, the second contains the photon counts.

[nm], [$\text{counts s}^{-1} \text{nm}^{-1} \text{cm}^{-2} \text{arcsec}^{-2}$]

Notes: Zodiacal light, and other background sources. If the wavelength coverage is incomplete, i.e. does not cover to the specified wavelength span, the missing values will be extrapolated.

exp

Exposure time

Integer.

[s]

Notes:

sub_pixel

Amount of sub-pixels per pixel

Integer.

[*sub-pixels*]

Notes: The full pixels will contain a number of sub-pixels equal to the square of *sub_pixel*.

wl_ran

Wavelength range

Tuple, 2 integers.

[nm]

Notes: Contains the first and last wavelength included in the simulation. As the simulator can only simulate a spectral resolution of 1 nm, the endpoints have to be whole integers.

eta_in*Total spectral throughput curve*

2D array, 2 columns, the number of rows must be equal to the wavelength span. The first column contains the wavelength, the other contains the fractional throughput.

[nm], [decimal fraction]

Notes: The input should be a combined Total Efficiency Curve (TEC), i.e. the spectral throughput of the entire system. It can strictly speaking also just be a single throughput curve. At least the CCD quantum efficiency should be supplied, but other aspects could be included, such as the optical throughput, chromatic effects from the spectrograph, etc.

slit*Size of the slit*

Tuple, 1 string, 2 floats. The string is the unit type, the floats are the size of the slit.

['unit'], [arcsec or pixels] eg. ['pix', 2, 3.5]

Notes: The 'unit' string can be either 'ang' or 'pix', corresponding to angular units or pixels. The two following integers should be the size of the slit. The program will use the plate-scale and the pixel size to convert to internal units (pixels) if the slit is given in arcseconds.

psf*Point Spread Function array*

3D array. The entries must be floats. It must have x- and y-dimensions of *img_size*×*sub_pix*. z-dimension is optional.

[relative intensity, normalised]

Notes: The user can opt to include several or all wavelengths in the *wl_ran*. If all colours are included, the *psf_col* input is not needed. Creating a simple model PSF can be done with the *psf_maker* function included in the simulator, see Section 6.3.1.

disper*Dispersion arrays*

2D array, 2 columns. The entries must be integers. The first column contains the x-dispersion per wavelength, the second contains the y-dispersion per wavelength. The array length must be equal to the wavelength span.

[pixel], [pixel]

Notes: Positions must be relative to the target position if no dispersion was present.

6.1.2 Optional inputs

jitter

Spacecraft jitter

2D array, 2 columns. The first column contains the x-coordinate, the other contains the y-coordinate.

[*pixel*], [*pixel*]

Notes: If the jitter is specified explicitly by the user, the input *step* is not used. The input must correspond to the exposure duration.

step

Time steps per second

Integer

[*steps s*⁻¹]

Notes: Only needed if the *jitter* input is not explicitly specified by the user: then the default (generated) jitter will be used. For more information about how this is generated, see Section 6.3.2.

psf_col

PSF wavelength list

Array. Must have the same length as z-dimension in the *psf*-input.

[*nm*]

Notes: Only needed if the supplied *psf* does not contain slices equal to the span of *wl_range*. The PSF values between these specified wavelengths will be interpolated, to achieve the correct number of slices.

in_CCD

CCD “imperfections”

2D array. It must be of the same size as *img_size* × *sub_pix*.

[*relative absorption sub-pixel*⁻¹]

Notes: Represents the sub-pixel-level imperfections of the CCD that arises during manufacture.

6.2 Simulator modules

With the input parameters in mind, the individual processes and inputs will be explained and explored in the following subsections. It is advisable to keep the flowchart (Fig. 6.1) ready at hand to follow the process. Some of the modules require inputs either specified by the user or generated by the auxiliary functions – such as the PSF or the spacecraft jitter. For an explanation of these auxiliary functions, see Section 6.3.

Each segment of the simulator – setup, image formation, and noise & read-out – will each, in turn, get a walk-through.

6.2.1 Setup phase

Before the actual simulation can begin, the inputs have to be the correct sizes in terms of wavelength, step-size, etc. All this is handled in the setup phase of the script. The setup phase consists of several steps – firstly, the input spectra are interpolated, in case the wavelength steps are not whole integers of nanometers. All of the spectral throughput curves will be interpolated to the correct sizes as well. Both of these are done using the *interp* function. After they have been interpolated, the spectral efficiencies are combined to form the Total Efficiency Curve (TEC). The spectral efficiency values can be thought of as spectral throughputs for different components of the system, such as the reflectance of mirrors, or quantum efficiency of the CCD. The TEC is the combination of all of these different efficiencies.

After the TEC has been formed, the input spectrum will be multiplied by the TEC and the collecting area of the telescope to create a scrambled spectrum. Once this is complete, the slit mask is created, along with the generation of a jitter array, if it was not supplied by the user.

6.2.2 Image formation

Now the simulator is ready to work on the most time-consuming aspect of the simulation - forming the detector image. When forming the image of the spectrum on the detector, several steps are repeated in a for-loop. First, the jitter-image and one of the PSF-slices will be convolved. This is to ensure that point-like stars are broadened out and that the effect of the ADCS is accounted for. This PSF-jitter image is then laid onto an empty array and the slit mask is overlaid. The PSF-jitter-slit image is then dispersed a number of sub-pixels equal to the *disper*-values of the corresponding wavelength. After that, the loop repeats itself and the next PSF-slice (wavelength) is folded with the jitter, etc. This is done for every wavelength step and each resulting image is combined as the loop repeats itself, see Figure 6.1.

When all colours have been run through the loop, there can be added a background noise multiplied by the exposure time to mimic the effect of zodiacal light.

Convolution

Before the spectrum is dispersed, the PSF and the jitter will be combined by convolution. Mathematically speaking, this means that the two inputs are shifted into Fourier space and multiplied. In the script, it is handled by the function `scipy.signal.convolve2d`¹.

Slit

The slit function of the simulator creates a mask to overlay the image. It has the same dimensions as the image, but is zero everywhere except for the designated slit area (see Figure 6.2), to mimic the effect of a physical slit in front of the optics in a real-life example. The function includes a position argument to change the location of the centre of the slit.

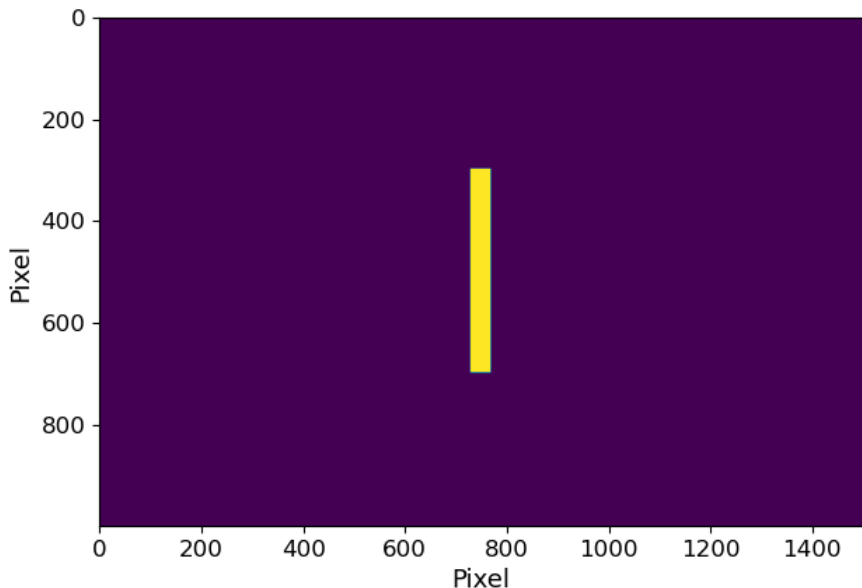


Figure 6.2: Example of a slit mask, with dimensions 20×200 , on a detector of 1000×1500 pixels.

¹<https://docs.scipy.org/doc/scipy/reference/generated/scipy.signal.convolve2d.html>

Dispersion

Many of the steps mentioned earlier are technically handled in the *disperser* function of the script, such as the slit-mask overlay. When it comes to the actual movement of the PSF-jitter-slit image, the module uses a function from Numpy, called *numpy.roll* that allows the user to shift array elements². The function essentially rolls the PSF-jitter-slit image the amount specified in the *disper* input array. Should there be a non-integer amount of dispersion, the module can also handle that, by moving a fraction of the “light” into the next sub-pixel.

6.2.3 Noise and read-out

After the dispersion and image formation is complete, the next module can handle the addition of different types of noise, sub-pixel summing, etc. Should the user wish to include more types of noise, the dispersed image can also be treated as the final output and be processed as such in further analysis.

CCD sub-pixel variations

To account for the unintentional manufactured variations on the sub-pixel level of the CCD, an image is multiplied by the input CCD-array. If the user does not specify an input but wants to include it, an array can be generated using the *CCD_maker* function described in Section 6.3.3.

Background noise

To include background noise in a simple way, a separate sequence of the image formation phase is run – this time with the zodiacal light’s spectrum instead of a stellar spectrum. The end result of this run will be a 2D image of a 1-second exposure of the zodiacal light, that can then simply be multiplied by the input exposure time and added to the dispersed image from before.

²For the full documentation on the function, see <https://numpy.org/doc/stable/reference/generated/numpy.roll.html>

Sub-pixel summing

So far, there has only been operated and manipulated on sub-pixel level. In order to truly see the incoming light as the CCD would detect it, the sub-pixels have to be summed up into full pixels. This is done by the `bin_sum` function. It takes two arguments: The input image (a 2D array) and the bin size – the bin size should be a whole divisor of the shapes of the image, otherwise there will be leftover sub-pixels.

The function sums over the x-direction first, taking care only to sum over the range $x : x + \text{bin_size}$, where x increases by the bin size over each “pass” of the image. When all bin size ranges are covered in the x-direction, the same process will be done for the y-direction. For a sketch of the process with 6×6 sub-pixels and a bin size of 3, see Figure 6.3. The resultant image is 2×2 pixels.

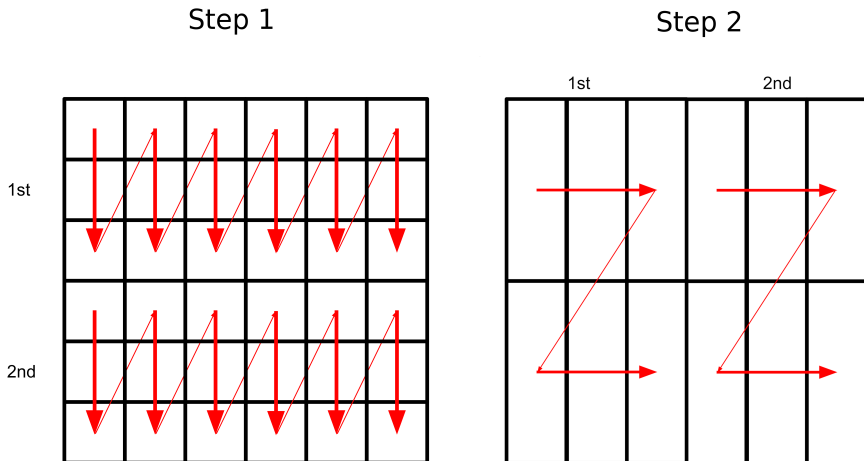


Figure 6.3: Illustration of the sub-pixel summing process. First, each column segment is treated, where the number of rows being summed is the bin size. After that, each row will be processed in a similar matter.

6.3 Auxiliary functions

Finding appropriate values for some of the input parameters needed to run the simulator might not be easy, so to assist users the auxiliary functions were made. They comprise of code snippets that might prove helpful in generating (somewhat) realistic inputs. All of these functions can be run outside of the simulator, by first importing the file containing them and then calling them with the correct arguments.

6.3.1 *psf_maker*

The *psf_maker* can as the name suggests, create a PSF for the user to supply to the simulator. The arguments needed are a filename in order to save the output, the desired wavelength range, and the size of the PSF in sub-pixels. The function returns a message of confirmation if the file was created. It can subsequently be loaded into the user's script or directly in the simulator. The function will create a 3D array containing the PSF in a wavelength span specified as a variable. The PSF generated will be a two-dimensional Gaussian distribution – with the full width at half maximum as a specified variable.

Each point in the x-y plane contains the value of the PSF – a representation of the likelihood of a photon striking that specific location – and each slice of the array contains the PSF for a specific wavelength. For a visual representation of a simple PSF-array, see Figure 6.4.

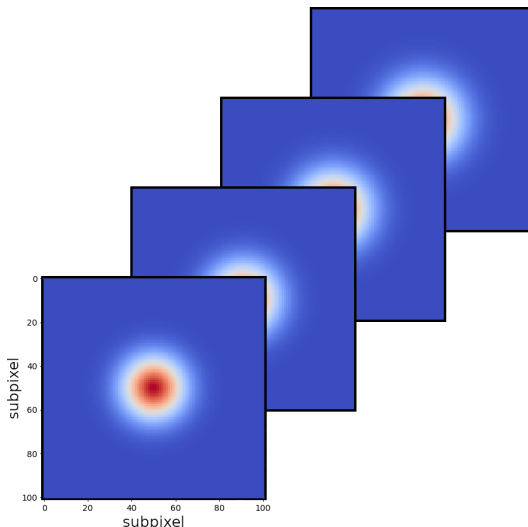


Figure 6.4: An illustrative view of select slices in the PSF array. As wavelength increases, the PSF should get larger due to diffraction.

6.3.2 func_jitter

This function can create the necessary jitter-array and it is automatically called if the user does not supply an array themselves. In order to simulate the spacecraft jitter, Equation 3.4 is used. The inputs of the function are the desired size of the output arrays, the gain of the correction, and the time delay of the system. Two arrays are created, one for each direction (x and y).

To have a benchmark to compare the generated jitter with, the reported pointing control of the ASTERIA CubeSat (Knapp et al. [2020]) is used. It can be seen on Figure 6.5. The mission reported a pointing RMS of 0.5 arcseconds over a time span of 20 minutes (e.g. Smith et al. [2018]).

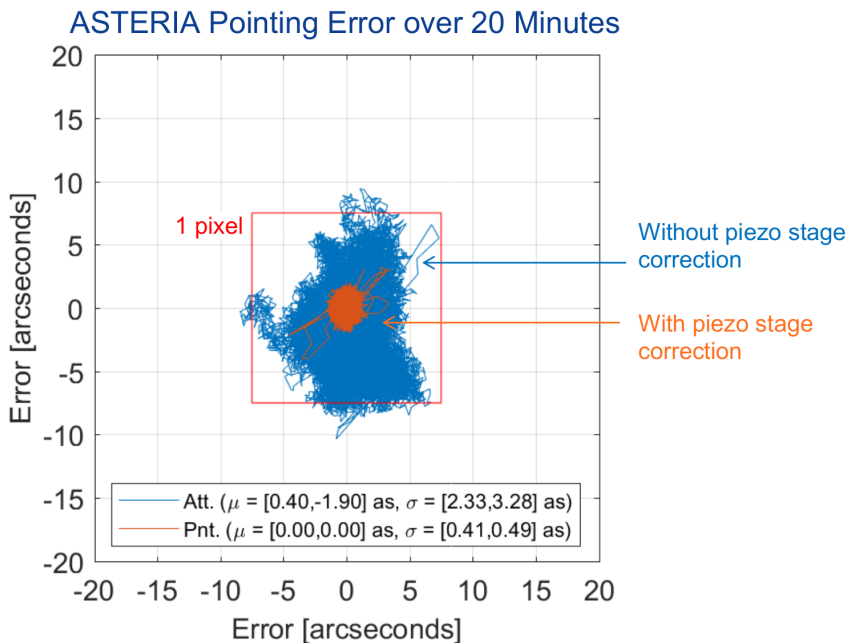


Figure 6.5: Jitter error of the ASTERIA CubeSat. The team used a piezo-stage to account for minute pointing errors, resulting in some of the best pointing accuracy to date. From Smith et al. [2018].

While this pointing accuracy is impressive, it might be more realistic to aim for something slightly lower. The pointing error of the generated jitter with the *func_jitter* (using default gain and time delay) is in the order of ~ 1.37 arcseconds. An example of some generated jitter can be seen on Figure 6.6.

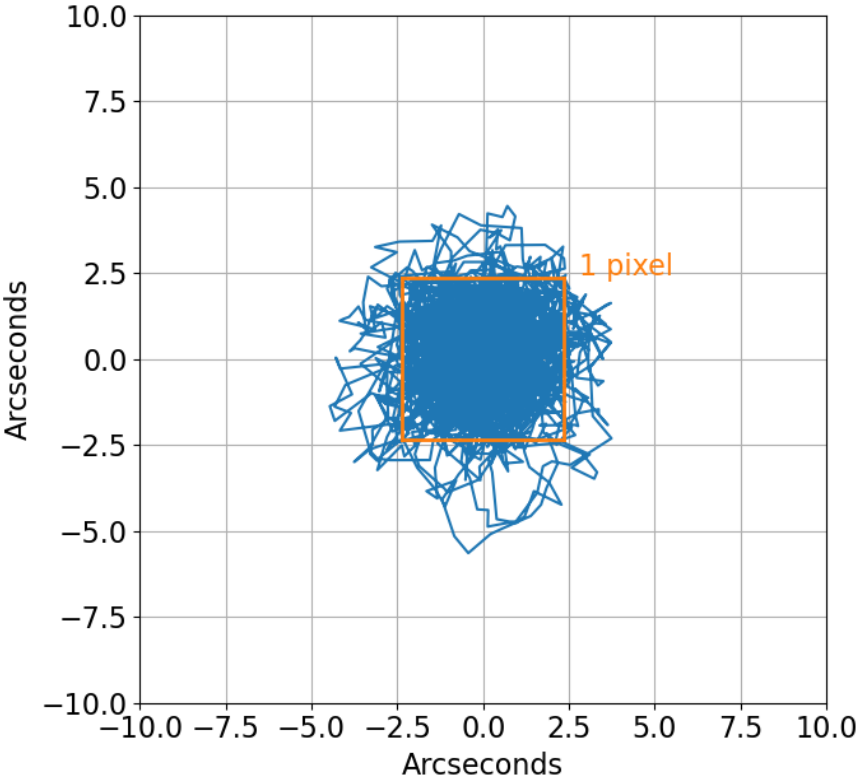


Figure 6.6: Generated jitter with 3000 steps (corresponding to 300 seconds, with 10 steps per second), using the default values of the `func_jitter` function. 1 pixel is drawn in orange. The size difference compared to that drawn in Figure 6.5 is due to a smaller field of view.

6.3.3 *CCD_maker*

The CCD and the inherent sub-pixel structure is also one of the inputs that can be generated – using the `CCD_maker`. This function will generate a single CCD by creating an array filled with numbers drawn from a normal distribution with the mean being 1 and the variation being a user input. This is to simulate variation of the sensitivity from sub-pixel to sub-pixel. Then each subpixel in this array is then correlated to the surrounding sub-pixels, as to create some cohesion and remove the true randomness of the generated numbers. In a real CCD, the sub-pixels will, at least to some extent, be similar in sensitivity to the nearby ones.

After the correlation, another array similar to the first (albeit with less variation) is added, and a grid is then overlaid to simulate the pixel gate structure. The decreased QE of the gate structure is included by having lower values in the grid. A small sample CCD generated with the function can be seen on Figure 6.7.

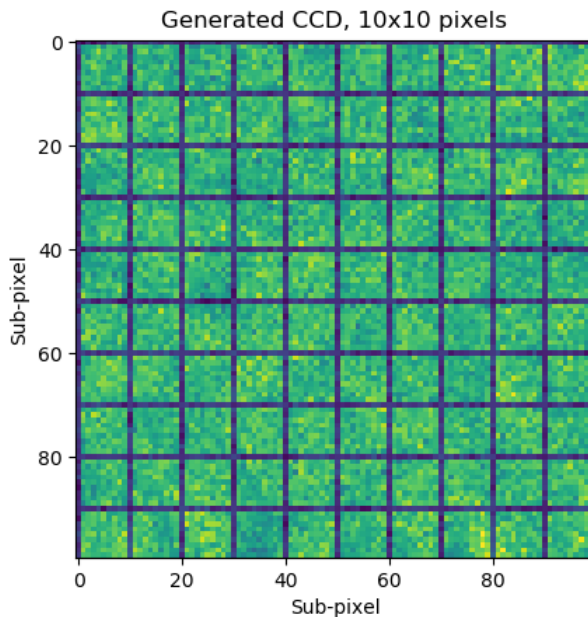


Figure 6.7: Generated CCD, consisting of 10×10 pixels, with 10 subpixels per full pixel.

6.3.4 *read_out*

As an extra, helpful function, a read-out function was created to more easily handle the comparison of output spectra. It simply takes a 2D array and collapses it into a 1D array by summing each column. In the following sections, whenever a 1D-spectrum is shown, it has been treated by this *read_out* function.

Simulator testing 7

In order to ensure that the simulator is working as intended, a testing scheme is set up so the individual aspects are verified, as well as the simulator as a whole. The overall structure of the test-plan is as follows:

- Test the interpolator.
 - Use two different sets of data, and compare the input and output.
- Verify the convolution of the PSF and jitter image.
- Test the disperser.
 - Try different dispersions in both directions.
- Ensure that the exposure time scales the output counts linearly.
- Verify that the binning of pixels works as intended.
- Test the simulator as a whole.

7.1 Input interpolator test

In order to verify that the interpolator work as intended, a few examples of inputs are interpolated and compared to the original inputs. Ideally, the new arrays should be in the specified wavelength range and have a number of steps equal to the step size times the wavelength range – the default being from 300-1000 nm. Using two sets of relative spectral throughput per wavelength as test values, the result can be seen in Figure 7.1. Two different sets of wavelength spans have been used (350-1000 nm and 400-1150 nm, respectively). The best kind of interpolation is dependent on the input, number of entries, etc., so it should be determined manually by the user for the best result.

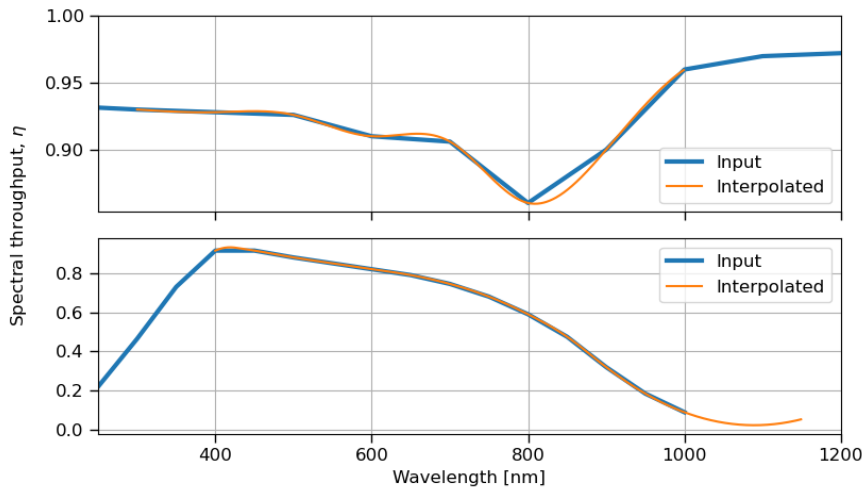


Figure 7.1: Test of the interpolation-function, using different kinds of interpolations, and different minima and maxima values. Top: cubic interpolation. Bottom: quadratic interpolation.

7.2 Convolution of PSF and jitter

To verify that the convolution of the two images (jitter-“image” and the PSF) works as intended, the function is given two samples and the result is examined. The test result can be seen in Figure 7.2. As can be seen, the convolved image retains the shape of the PSF, but with the asymmetric aspect of the jitter imposed. This is evident from Figure 7.2.D.

If the convolved image had been a perfect two-dimensional Gaussian – like the PSF – the two cross-cuts spaced evenly from the centroid should have been identical. In general, their similarity is heavily dependent on the supplied jitter image. The convolved PSF-jitter image looks as expected and it is concluded that it works as intended.

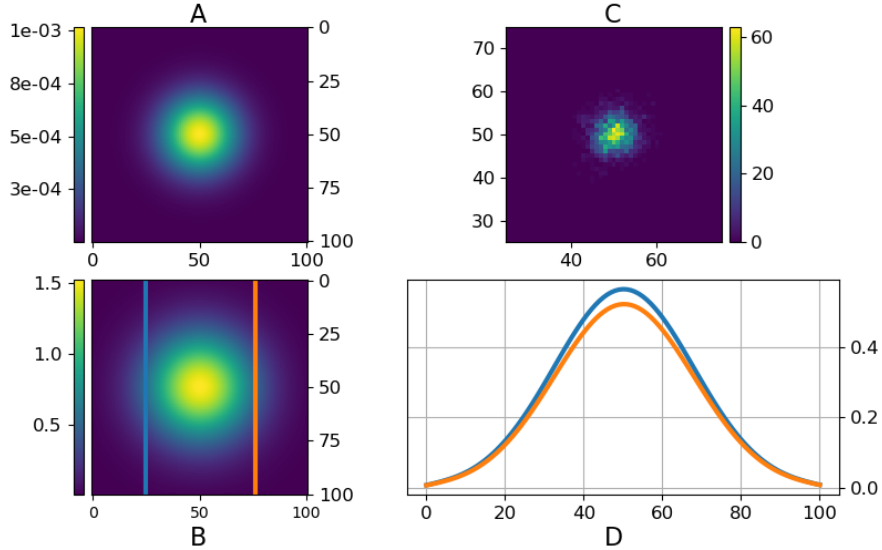


Figure 7.2: Testing the convolution of two images. **A:** Sample PSF, a 2D Gaussian. Made using the *psf_maker*, see Section 6.3.1. **B:** Jitter, zoomed in (note the asymmetric shape). **C:** Convolved PSF-jitter image. **D:** Two cross sections of the convolved image at $x = 25$ and 75 to show the asymmetric shape of the Gaussian-like image.

7.3 Dispersion test

To test the disperser, a simple scheme is set up. Both the dispersion in the x- and y-direction needs to be verified, as well as movements in non-integer sub-pixel amounts. To start, just the x-direction will be tested, then only the y-direction, and then both. While testing the dispersion, all other parameters will be effectively turned off; every entry of the PSF array is set to 1, in all colours; jitter is turned off; the slit mask is left entirely open; the input spectrum is uniform (and left at a spectral throughput of one). The test results can be seen on Figure 7.3. If no dispersion is used (Fig. 7.3.A), all of the convolved jitter-PSF images will be layered in the same location, hence the high values of the cross-section (700 in all the non-zero pixels).

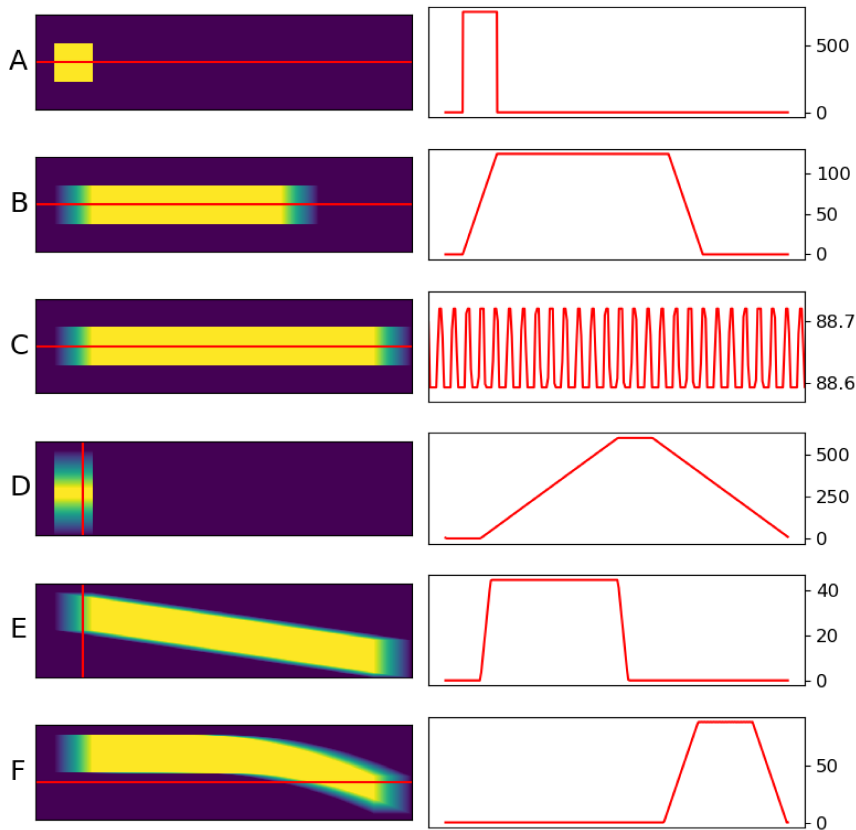


Figure 7.3: Dispersion tests. The left column shows the resulting image, while the right column shows the cross section marked in red, with the counts shown on the ordinate. **A:** No dispersion. **B:** Only dispersion in the x-direction of integer amounts. **C:** Only dispersion in the x-direction, in equidistant but non-integer amounts. The cross section shown is zoomed in on the plateau. **D:** Only dispersion in the y-direction. **E:** Dispersion in both directions. A combination of C and D. **F:** Dispersion in both directions. Same x-dispersion as C and E.

Whole integer dispersion in the x-direction (Fig. 7.3.B) looks as expected: Initially, there is a sharp increase in the intensity, then the intensity is constant throughout most of the dispersion, and ends off with a sharp decrease. This corresponds to some of the convolved jitter-PSF images getting inserted at the beginning and then they start to overlap more and more until the peak intensity is reached. In the end, they start to overlap less and less.

Equidistant but non-integer dispersion in the x-direction (Fig. 7.3.C) has small variations in the intensity, arising from the jitter-PSF images overlapping more at some of the subpixels than others. The same effect is visible in Fig. 7.3.E - F, although it is not shown explicitly. It is also expected to be seen if the dispersion is increasing non-linearly.

Dispersion only in the y-direction (Fig. 7.3.D) is also as expected: An increasing intensity, until a peak is reached and then a decrease, as seen in the x-direction.

Both directions in the dispersion (Fig. 7.3.E), looks like a combination of the previous examples, as intended. When introducing non-linear y-dispersion (Fig. 7.3.F), it still looks like expected. Visually, the bottom right part of Fig. 7.3.F, there appears to be less intensity and this is an effect of less jitter-PSF images being stacked.

While the disperser works in a simple manner, it is concluded that it works as intended.

7.4 Exposure time

The exposure time is incorporated into the jitter function – if one wishes an exposure of 10 seconds, the user should also specify the number of steps per seconds, and the jitter should have the length of the product of the exposure and step size. So if the exposure is 10 seconds and the step size is 10 steps per second, there will be 100 entries in the jitter array. To quickly generate an appropriate jitter-array, see Section 6.3.2. This is tested by doing two exposures of 1 and 2 seconds with 10 steps, and checking whether the output spectrum of the second exposure has twice the photon count of the first. For this test, the PSF will be left in the same configuration as in the disperser test, so every entry of the PSF array is set to 1, in all colours. The jitter is turned off and the slit is left entirely open, the same settings as for the disperser test. The spectrum used is a sample spectrum, to show how exposure affects the shape.

The total photon counts of the 2-second exposure should be equal to twice the total photon count of the 1-second exposure. It is also tested for an exposure of 30 and 100 seconds, which should simply be scaled with respect to the first exposure. See Figure 7.4 for the read-out for the first two exposures. Indeed the sum of counts in the second exposure was equal to twice the counts in the first exposure, and for the 30-second exposure, this was **29.999999999999932** times the first exposure. This is for the intents and precision used, close to 30. For 100 seconds, the number was **99.9999999999997**.

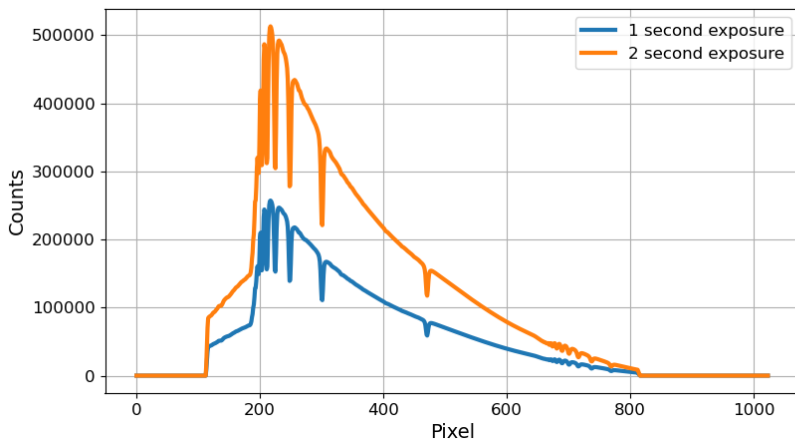


Figure 7.4: Exposure test. The output images have been collapsed to a 1D spectrum, by summing each column of the images, see Section 6.3.4.

This minuscule deviation from integer values might have arisen from rounding/floating-point errors during the dispersion etc. The test thus showed that scaling the exposure works as intended.

7.5 Sub-pixel to pixel summing

In order to make sure the sub-pixel summing process works correctly, a few different setups are tested. Different pixel sizes (in sub-pixels per pixel) are given – 5×5 (25) sub-pixels, 10×10 (the default amount), and 20×20 (400) sub-pixels. An example of a binning and summing can be seen in Figure 7.5. The mean value of pixels in the original image is 114.7749, where the processed image mean pixel value is 45909.946, which is 400 times the original (20×20 sub-pixels).

Thus it is concluded, by using ordinary pictures, that the *bin_sum* function works as intended: It sums up sub-pixels in the correct bin sizes.

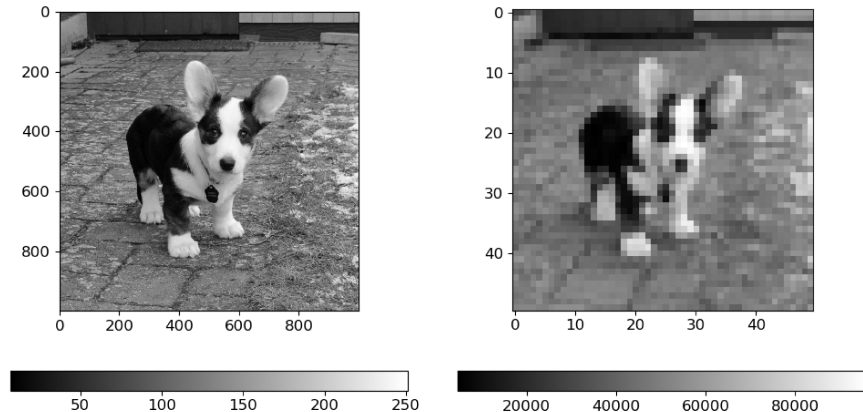


Figure 7.5: **Left:** Original image. **Right:** Same image, treated by the `bin_sum` function, with bin size 20. Note that despite the colour seems the same, the pixel values are much higher in the processed image, as shown in the colour bar below.

7.6 Concluding remarks on testing the simulator

The entire simulator as a whole is also tested as a semi-redundant insurance. The result of a regular run of the code using sample values can be seen in Figure 7.6. After the simulator was completed, the 2D spectrum was collapsed into a 1D spectrum by the `read_out` function, summing all columns. The spectral absorption lines can clearly be seen, and the overall Planck-spectrum shape is also visible. It should be noted that the overall shape is affected by the spectral sensitivity, η , of the system – optics and QE of the CCD, in this sample.

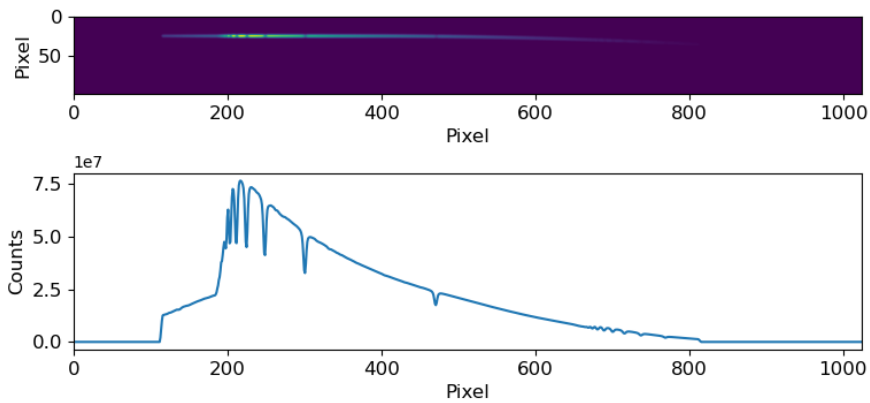


Figure 7.6: Sample run of the simulator. A 300-second exposure, with “standard values”, but no noise or background. Jitter RME ≈ 1.3 arcseconds, and a slit of 1 pixel wide.

Given that all of the tests came back as expected, it can be concluded that the simulator is relatively robust (given sensible input values) and can handle a variety of different input specifications.

Simulating a spectrograph 8

Now that the simulator has been explained and its modules tested, an actual run seems appropriate. For this, two stellar spectra has been supplied, see Figure 8.1 – one of includes an exoplanet with an atmosphere transiting the star. The objective is to determine whether it would be possible to detect an exoplanetary atmosphere, given sensible parameter inputs and realistic benchmarks.

8.1 Simulator inputs

The spectra are of an zeroth-magnitude A-type star, and the planet is a hot Jupiter. The spectrum is made using SPECTRUM¹, a synthetic stellar spectrum generator run in *C*. The atmosphere of the exoplanet is based on the models in Fortney et al. [2010]. The spectra was pre-processed by Victoria Antoci (hereafter VA).

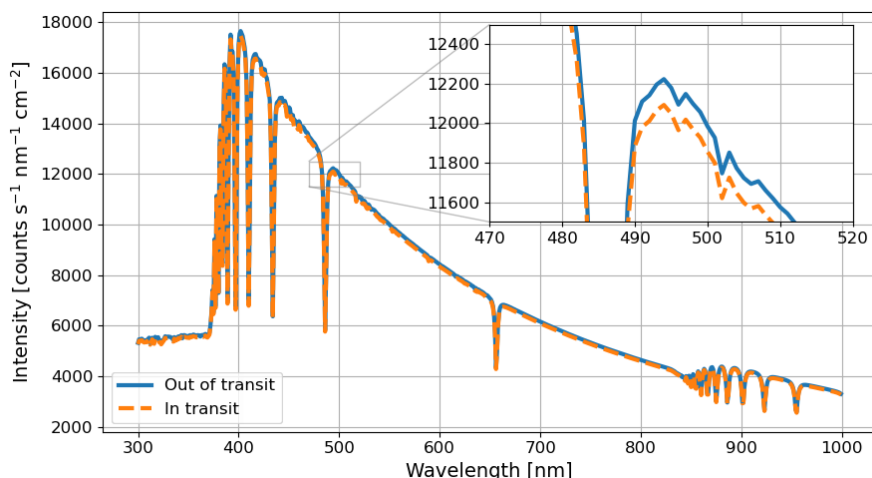


Figure 8.1: Input spectra, both with the exoplanet in and out of transit. Supplied by VA.

¹<http://www.appstate.edu/~grayro/spectrum/spectrum.html>

To get a realistic baseline for the CCD, the values used for this simulation is that of a Teledyne e2V CCD42-90². It is a back-illuminated, low-noise CCD, composed of 2048×4612 pixels, with a pixel length of $13.5 \mu\text{m}$, ideal for a satellite mission for astronomy. Some of these pixels could be used for Full Frame Transfers, or background detection, etc., but given that such a large detector would only serve to slow down the simulator, only 1024×100 pixels are considered further in this analysis. Concerning the other parameters, the CUBESPEC and ASTERIA satellites are used to get decent baseline values for the inputs, such as telescope size, ADCS mean precision, etc. The values used in the simulation can be seen on Table 8.1.

Parameter	Value
in_spec	See figure 8.1
wl_ran	300-1000
col_area	200 cm^2
img_size	1000×100
pl_scale	$355.63 \text{ arcsec mm}^{-1}$
pix_size	$13.5 \mu\text{m}$
exp	300 s
PSF FWHM	3 pix. @300 nm
sub_pix	10 pixel^{-1}
eta_in	See figure 8.2
slit	variable
jitter	1.3 arcsec (RMS)

Table 8.1: Input parameters used in the simulation.

The slit of the system in this test is left variable, so to asses the effects of it during the simulation. The width of the slit is set to one of the following sizes: 1, 2, 4, and 12 pixels, corresponding to 4.7, 9.4, 18.8, and 37.6 arcseconds, respectively. In order to get meaningful results, and to ensure that the simulator did not simply got lucky with the jitter, the simulator is run 20 times, 10 for the spectrum without the exoplanet, and 10 with it. When varying the slit-width, the same 20 jitter arrays are used, so the first run of all the different slit-widths use the same jitter, and so on.

²Full data-sheet available at <https://www.teledyne-e2v.com/markets/space/astronomy-imaging/ccd42-90-and-ccd44-82/>

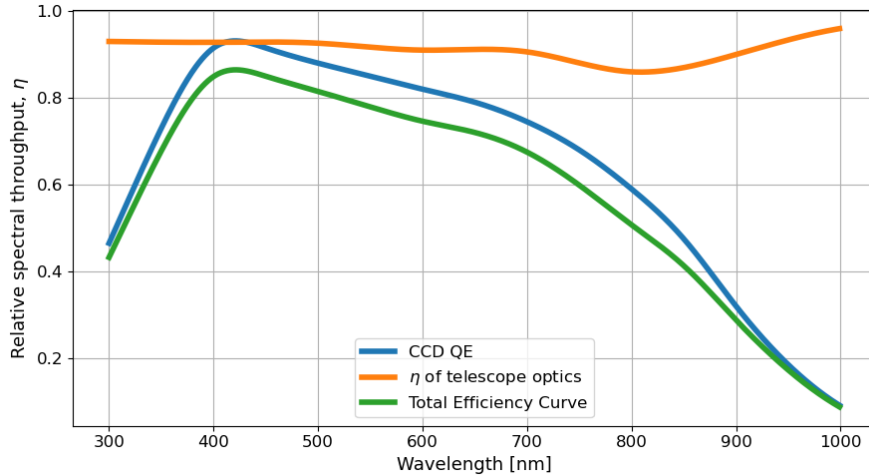


Figure 8.2: Spectral throughput used in the simulation shown in green. The throughput of the spectrograph itself is not included yet, but generally the overall throughput of such is low (in the order of 20-25%).

8.2 Method, results and discussion

The simulation is run in pairs with the two spectra and they are immediately compared, by plotting the transmission spectrum, like described in Section 2.2.4. A single simulation output prior to any further processing can be seen on Figure 8.3.

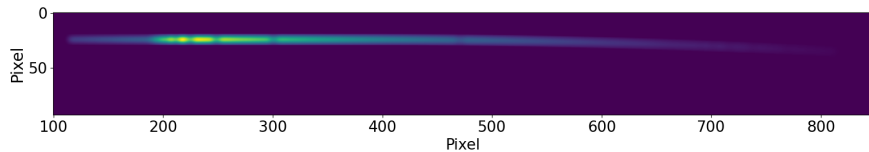


Figure 8.3: Output of a single simulation without CCD imperfections and noise.

The transmission spectrum is the difference between the outputs, normalized by dividing by the out-of-transit spectrum. Such an output transmission spectrum can be seen on Figure 8.4.

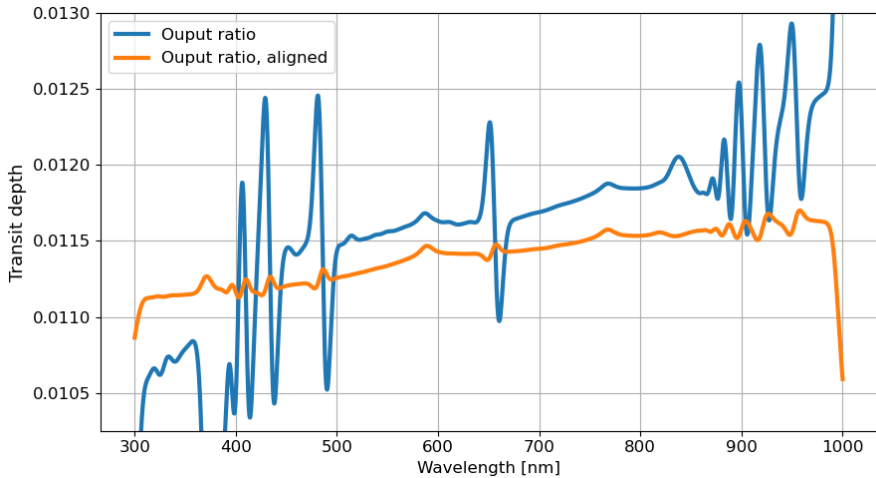


Figure 8.4: Normalized ratio of a simulation pair. Shown before and after being shifted to correct for misaligned pixels.

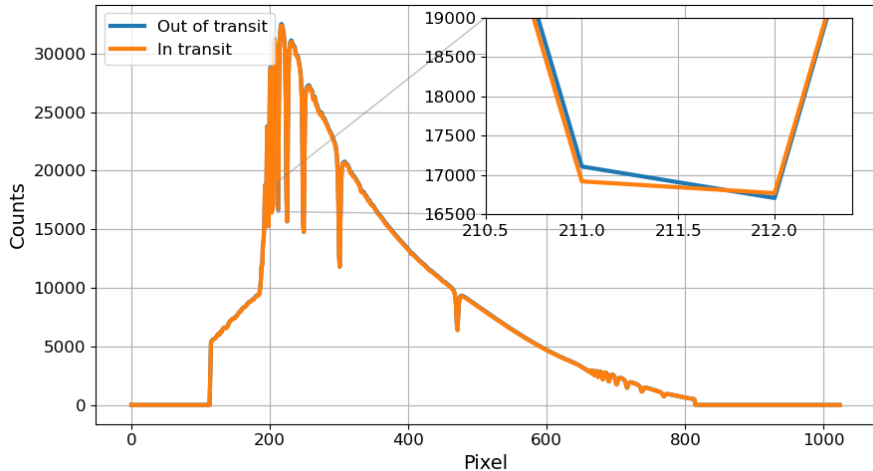


Figure 8.5: Output spectra, collapsed to 1D. The misaligned spectral lines are quite clear when zooming in. The reason behind this effect lies in the jitter.

As can be seen on Figure 8.4, the spectrum is shown with wavelength on the abscissa. To simplify the data-processing, it is assumed that the wavelength calibration is known – in this specific case, the dispersion-array is simply used to calculate the corresponding wavelength of each

pixel and the conversion is made. In a real-life scenario, a ground-based setup might include a light source, such as a thorium-argon lamp, with many well-defined emission features, to find the corresponding wavelength/pixel conversion. In space-based missions, stars with known spectra are often used for calibration purposes.

Figure 8.4 show some large sudden peaks, varying quite a bit in both positive and negative direction. These arise due to misalignment of the two output spectra, especially near deep spectral lines, such as H α (656.279 nm) and H β (486.135 nm). A pair of simulations with the effect clear can be seen on Figure 8.5.

To account for the worst of this effect, one of the spectra can be shifted to better align them. Before doing this shift, the resolution is artificially increased by interpolating over the spectrum, and the resolution is increased by a factor 100.

The shift of one spectrum is done by first auto-correlating one of the spectra, and correlating the two spectra with each-other. Then, the position of largest correlation coefficient in both cases are used to find the amount of sub-pixels to shift one of the spectra, and the spectrum is then moved. An example of this shift can be seen on Figure 8.4. The data has also been smoothed by a moving mean filter to decrease the peaks further.

Even after this shift of one of the spectra, the peaks still persist. To check if it was not due to an error in interpolation (when increasing the resolution), the degree of interpolation was changed, so both linear, cubic, and 7th degree interpolation was done. This made no discernible change to the outcome. The exposure was also increased to 1200 seconds, to see if the peaks would decrease, but it had no clear impact on the ratio.

It was noted that the peaks were smallest in the simulations with a narrow slit, and it became clear that the effect is due to the jitter not being symmetrical (see Fig. 7.2.C). The asymmetrical jitter causes some of the light in the PSF-jitter image to be slightly shifted, and thus the light on the image-array might be shifted a tiny amount compared to the previous run – creating skewed spectral lines. The slit cuts of some of the PSF-jitter image (see Fig. 4.2) and it results in a “misplaced” image. If the simulation is run with no jitter, the same picture looks a lot cleaner, as can be seen on Figure 8.6.

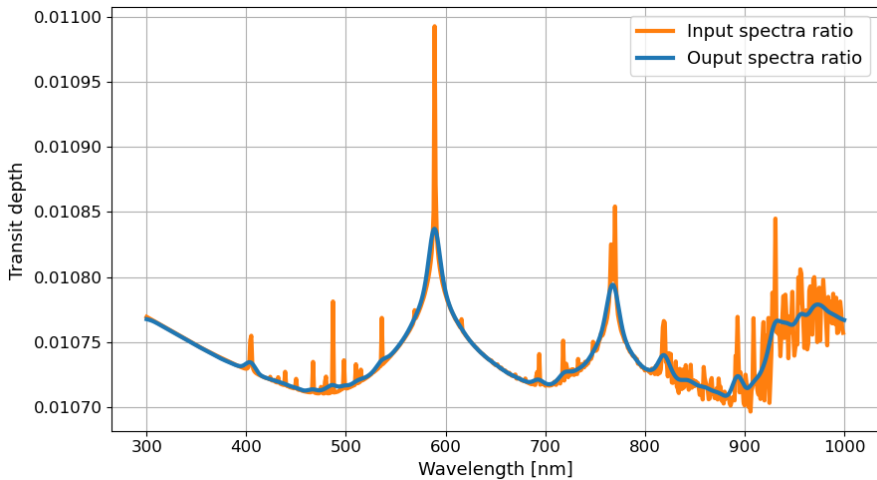


Figure 8.6: Ratio of a pair of simulations with no jitter enabled, overlaid on the input spectra ratio.

As can be seen on the jitter-less ratio, most of the features visible in the input spectra ratio are also discernible here. The main feature is the sodium double line near 589 nm, although the two lines are not individually resolvable. In the red end of the spectrum a lot of spectral features are visible in the input spectra, but in for the output, they are not resolvable – this is due to the low spectral resolution.

To properly compare the input spectra ratio (despite the misaligned spectral lines), the average of all 10 pairs of simulation runs will be plotted. This can be seen for a slit-width of 12 pixels on Figure 8.7.

The general shift of the transmission spectrum (the shift in the y-direction on the figures, e.g. on Figure 8.7) also arise due to the “jitter-defect”: If the jitter is consistently skewed in one direction (that is, if the jitter is consistently worse for one of the computations in a simulation pair, say for the out-of-transit spectrum) there might be a visible increase or decrease in the amount of light hitting the detector.

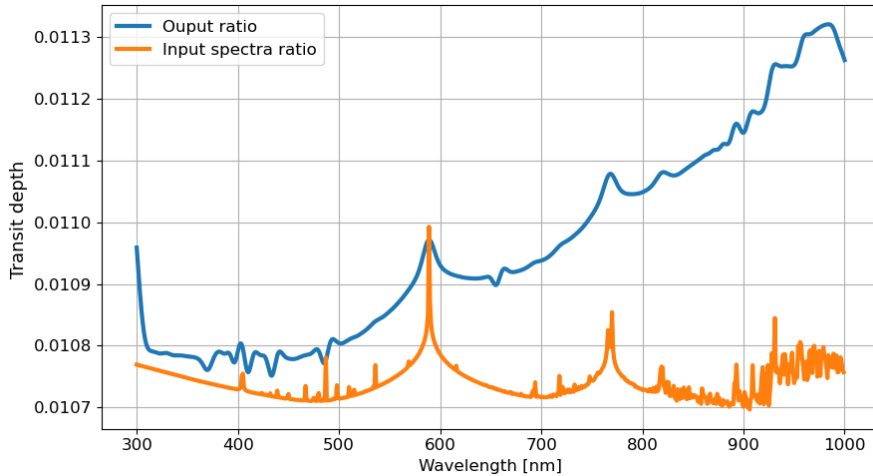


Figure 8.7: Transmission spectrum of the mean of all 2×10 simulations, with corresponding errors, of the 12-pixels wide slit. The untreated input transmission spectrum is also shown.

The ratio of the output will thus have a different value than the input. Seeing as these simulation sequences all use the same 20 jitter arrays, but have different slit-widths, the effect will vary over the different slit-width variations.

When comparing the sequences of more narrow slits to those of wider, it becomes clear that the open slits yield better results when compared to the input transmission spectrum. This is also the work of the jitter in combination with the slit: For more open slits, most of the PSF can pass unobstructed and so most of the light can hit the detector. For the case of narrow slits, a lot of the PSF gets excluded, especially so in cases with large jitter-values – resulting in generally larger variations. A comparison between the 2-pixel- and the 12-pixel-wide slit can be seen on Figure 8.8.

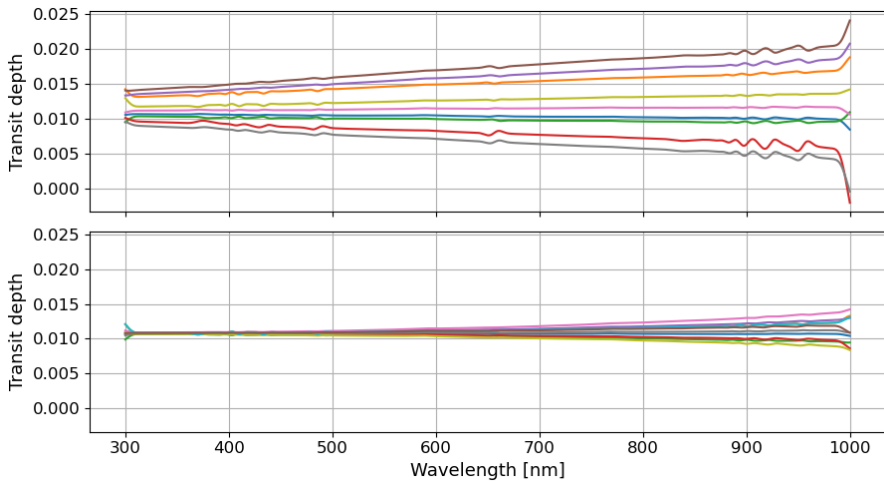


Figure 8.8: Transmission spectrum of every simulation run, for slit-width 4 pixels (top), and 12 pixels (bottom).

From this, it is quite clear that a more narrow slit (which would in real life increase the spectral resolution) mainly serves as a sources of variations and that the best results are then achieved by using an open slit.

There is a general trend of larger fluctuations in the red end of the spectrum, compared to the blue (see Fig. 8.8) – and once again the jitter is the culprit. As the PSF (which is larger in the redder wavelengths in this case) gets moved around by the jitter, more of the light will be excluded by the slit, than for the smaller PSF in the blue end of the spectrum. If the jitter then shifts the PSF so a significant part of the light in that wavelength will not be detected on the CCD, it will lead to changing intensities in the output spectrum. For different runs, with different jitter, this will lead to the largest variations in the red end of the spectrum.

To get rid of all these jitter-based effects, the simulation can be run enough times for the mean jitter image to be symmetrical. 20 jitter-arrays is obviously not enough, but due to time-constraints no more were tested. Otherwise, the slit could be left entirely open, and the telescope defocused (effectively enlarging the PSF). Such an attempt was made, where the PSF was effectively doubled in size (so the FWHM @300 nm was ~ 6 pixels) and disabling the slit entirely. This proved somewhat fruitful and the sequence of simulations can be seen on Figure 8.9.

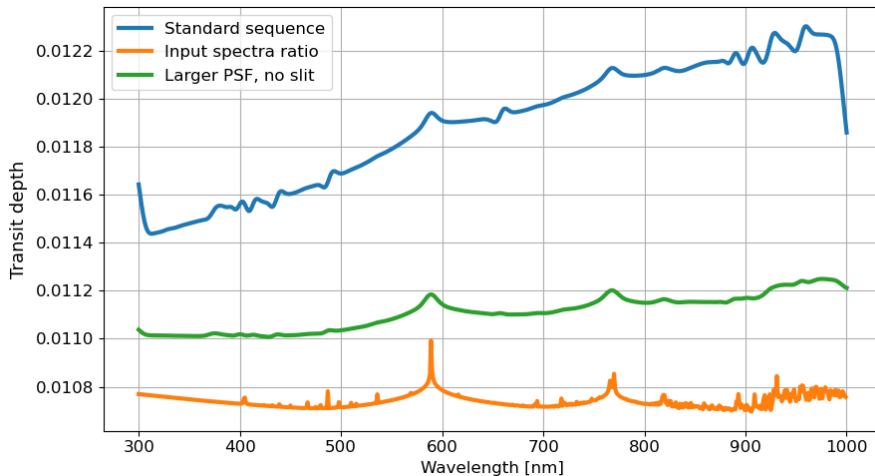


Figure 8.9: Mean of a sequence of simulations with enlarged PSF and no slit, compared to a regular sequence and the input transmission spectrum.

Given the more accurate output, these new settings are used from this point on. The same procedure has been done for this sequence as the previous: Ten pairs of simulations have been conducted, and the mean of all out-of-transit and the mean of all in-transit spectra are used. The open slit setup equivalent in an actual system would most likely be a grism, so the overall effective throughput of a grism is included in the final image: This is done by multiplying each image with the peak spectral efficiency of the Nordic Optical Telescope's ALFOSC grism³ 10, which is around $\sim 22\%$.

So far, no noise or CCD sub-pixel variations have been included in the simulation, and enabling these will muddle the otherwise the sharp peaks in the transmission spectrum plot. Only the CCD sub-pixel imperfections, photon noise, and read-out noise were included, but background noise and other noise sources could be included later. Figure 8.10 shows the output spectra ratio with the CCD-imperfections included.

³Found at www.not.iac.es/instruments/alfosc/grisms/

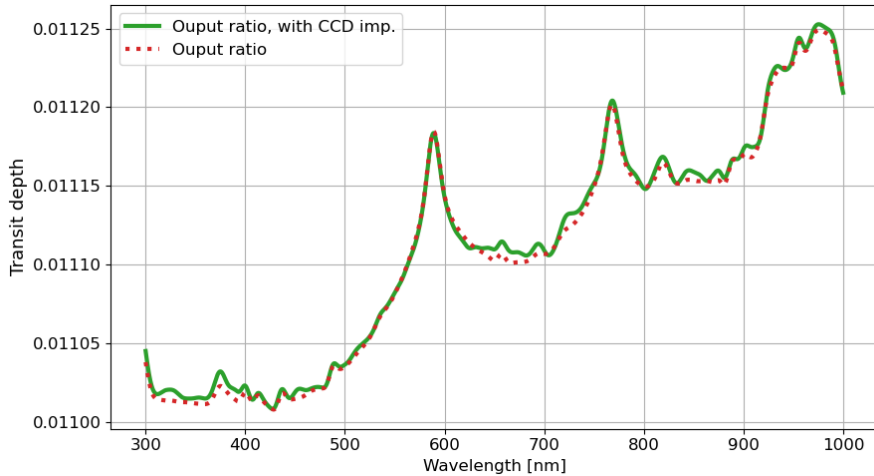


Figure 8.10: Output spectra ratio with CCD imperfections.

Although the CCD imperfections does not cripple the ability to detect the transmission spectrum features, it certainly does not help. When including noise (photon noise and read-out noise), the spectral features are even more difficult to discern. In general, all noise sources were handled in a quite simplistic manner. The following is an approximation of noise and is this not a definitive simulation of all noise sources. When treating the output image, a noise image is created and added. The noise values are created using the following equation:

$$\text{noise}_{i,j} = (\sqrt{N_{i,j}} + RON) \cdot \mathcal{N}(\mu = 0, \sigma = 1), \quad (8.1)$$

where $N_{i,j}$ is the photon count of the considered pixel in the 2D-spectrum, RON is the read-out noise, and \mathcal{N} is a random number drawn from a normal distribution with mean, $\mu = 0$, and standard deviation, $\sigma = 1$. From this, it follows that the noise is orders of magnitudes larger in the illuminated band on the detector, than in the non-illuminated band – seeing as the noise in this area will only be equal to the read-out noise. This equation is simply used for each entry in the 2D-spectrum, and the resultant image is added to the 2D-spectrum. To compare the noise of this particular case of a zeroth-magnitude star to a less bright object, the 2D spectrum can be multiplied by the appropriate factor. For a 5th magnitude star the spectrum is multiplied by 0.01

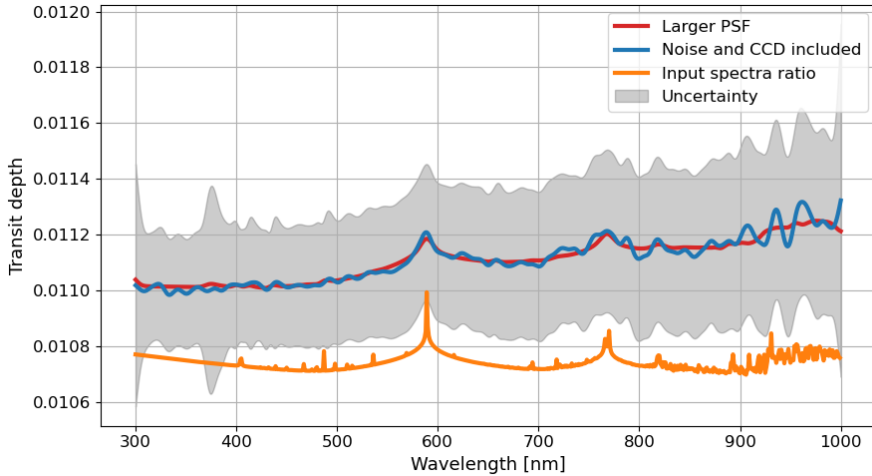


Figure 8.11: Transmission spectrum of the mean of the sequence of simulations with larger PSF and open slit, with noise and CCD imperfections enabled.

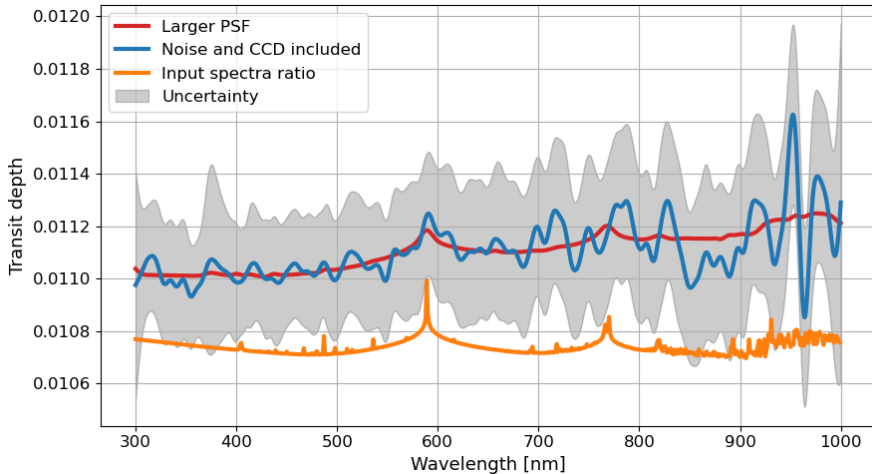


Figure 8.12: Transmission spectrum in the same setup as in Fig. 8.11 but with a 5th magnitude star (i.e. 1% as bright).

With the noise added to each of the 20 simulations, and finding the mean of the out-of-transit and the in-transit sequences, the transmission spectrum is found as per the already established method. The result can be seen on Figure 8.11. As can be seen on the figure, the large

spectral features are in fact discernible in spite of the added noise. The uncertainties are still quite problematic, but can be decreased by increasing the exposure time or taking the mean over more simulations. It is calculated for each entry in the array by the equation:

$$err_i = \sqrt{\frac{1}{\tau} \cdot \left(\frac{\sigma_{out, i}^2}{\mu_{out, i}^2} + \frac{\sigma_{in, i}^2}{\mu_{in, i}^2} \right)}, \quad (8.2)$$

where τ is the number of simulations in the sequence (in this case 10). σ^2 is the variance of the i -th value of all τ simulations in either the out-of-transit or the in-transit simulations, as described by the sub-script. μ is the mean value of the i -th entry of those simulations.

This is equal to 1σ uncertainties and as can be seen from Figure 8.11, the main problem is the current off-set in the transit depth. Defocusing the setup even further should minimize this off-set considerably. It should be expressed that these uncertainties are in absolute values, and they can thus only be used to evaluate the global position of the transmission spectrum. The relative uncertainties, which would be used to evaluate the spectral lines, are much lower as the general shape of each output spectrum could be subtracted. A way to do this would be to fit a curve to the general slope of the transmission spectra (see e.g. Fig. 8.10) and removing it from the spectra, before finding the mean of the simulation sequence.

The current uncertainties could be used to evaluate whether effects like Rayleigh scattering (from clouds, hazes, etc.) is present in the exoplanetary atmosphere. Given the uncertainties of Fig. 8.11 and 8.12, it seems like there is no such effect present. From private conversations with VA, this was also confirmed.

From the simulations, it is concluded that in order for the given setup to detect the exoplanetary atmosphere, the jitter should be very well constrained. It is determined that with a larger PSF and open slit, the effect of the misaligned spectral features is less prominent – which is necessary to detect the exoplanetary atmospheric features. Including some of the noise-sources makes for less discernible features, but with the main spectral feature – the sodium doublet – still being detectable, as well as the overall shape of the output spectra. Thus, it is deemed most optimal for the given telescope and detector to use a low-dispersing, open-slit setup – a grism seems most appropriate in this context.

Future improvements 9

In this chapter, some of the consideration when making the simulator are discussed, and a few possible improvements are listed and briefly explained. This section is meant to be a list of potential ways to improve on the current simulator and make it more useful and/or faster.

Secondary light sources

It should be possible to include contamination of the spectrum from other light sources than the primary. A simple way to include the effect would be to change the PSF to have a secondary light source (hopefully smaller than the primary) somewhere near the border. Then, there are two ways to include the effect from this point: Either, the spectra of both light sources are simply combined, or the simulator is run twice with the different spectra and then combined afterwards. An example of a combined PSF can be seen on Figure 9.1.

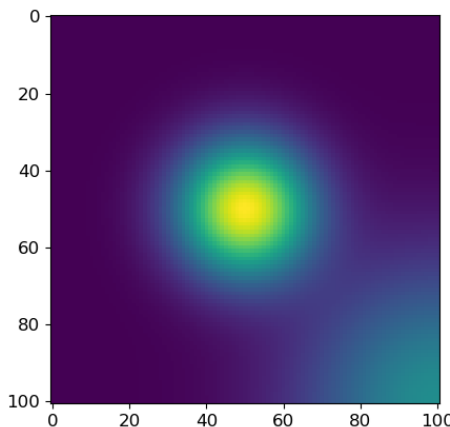


Figure 9.1: Sample PSF with a secondary light source in the lower right corner. Such a scenario might arise due to the target star being angularly close to the background star.

Higher spectral resolution

Currently, the simulator incorporates the wavelength variations with a for-loop. This means it can only take whole integers of wavelength – in this case, that means nanometres. This was chosen during the writing of the Python-script, mainly to keep the simulator simple and light enough to run on an average laptop. In theory, one could simply scale up the for-loop to have an even better resolution – the only caveat being, the runtime would rapidly increase as well. The current runtime is in the order of ~ 6 minutes (with a wavelength span of 700 nm – 700 loops), so increasing the resolution to Ångström-level would increase the runtime upwards of one hour. The runtime is *per run* and to get some meaningful results, the simulator should be run multiple times. Such long runtimes are in general not in the interests of the average user. Ideally, a faster way to incorporate different wavelengths should be explored. One way to speed up the simulator could be implementing it in the *C*-programming language – often this language is faster than Python¹.

Better convolution

In the current simulator, the PSF and jitter are combined through a convolution, the mask is added, and it is subsequently placed on the otherwise empty image-array. In a more representative scenario, the PSF-jitter image should be convolved with the entire image-frame with the target star (and other potentially contaminating sources) and then the slit-mask could be added. This was not done, as the convolution can slow down the simulator. If a faster alternative – or a technique just as fast, but more “true to nature” – could be found the simulator would be better by it.

Synchronous pan-chromatic illumination

The simulator current handles each wavelength step separately, adding each image to the empty image-array, while a real-world system illuminates the entire spectrum at once. Incorporating this style of rendering the spectrum would make the simulator more realistic in a sense, but the end result would most likely not change significantly, which was one of the reasons why it was deemed non-essential for this simple simulator.

¹C is at least 10 times faster in most cases, <https://peter-jp-xie.medium.com/how-slow-is-python-compared-to-c-3795071ce82a>

Dispersion

The spectral resolution is one of the limiting factors and the dispersion suffers slightly under it. If the spectral resolution could be increased, new and more often used dispersions could be implemented – such as a high-resolution cross-dispersion from an echelle spectrograph.

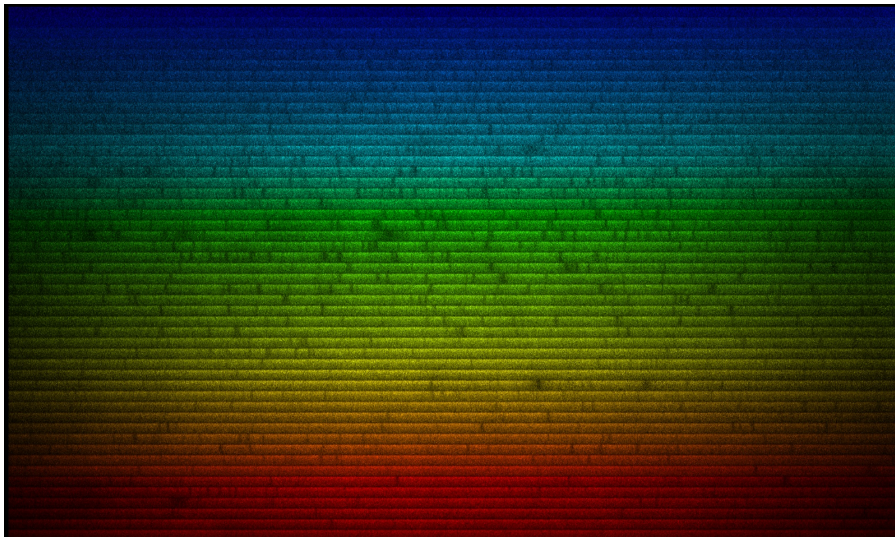


Figure 9.2: Typical Sun spectrum from the danish Hertzprung SONG telescope. The colours are artificially added to illustrate different orders. From <http://song.phys.au.dk/>

Many current and proposed missions, both ground-based and in space, use/will use echelle gratings to increase their spectral resolving power (see e.g. the SONG telescope, Grundahl et al. [2008] or CUBESPEC, Raskin et al. [2018]). Including this feature of more “exotic” dispersion could, in theory, be added by simply using a larger image-array and having the appropriate dispersion-array – but the spectral resolution should be increased prior to this.

Better error-checking

The current version of the simulator has very little in terms of input format-checking, i.e. raising an error if the input is not in the correct format or type. This could prove troublesome if a user supplies one of the inputs in an incorrect format. Although somewhat tedious, implementing functions to check the inputs would be simple and is only partially included in the setup phase of the simulator.

PSF improvements

The current *psf_maker* function can generate a 2D-Gaussian distribution, but there already exists libraries for generating these² – including Airy discs, among other shapes. Implementing these variations of the PSF could prove more true to nature, without imposing considerably longer computation times.

Cosmic rays

A possible addition to the simulator would be a module to generate cosmic rays and energetic particle streams in general. Seeing as these events are not uncommon, examining the effect of these events on a detector and the subsequent quality of data, would be an interesting case for further consideration.

FWC

Currently, the simulator has no way to handle pixels potentially bleeding photons as seen in saturated images. There are several ways to handle this issue in real CCDs, such as anti-blooming gates (see e.g. Howell [2006]). Implementing this would make the simulator better suited to handle very bright objects more correctly, as very bright stars might saturate pixels.

²Such as the *astropy* library for Python.

Conclusion 10

In this thesis, the scientific study of exoplanetary atmospheres was used as a background for the creation of a simple simulator of a detector in a spectrograph setup. A general introduction to exoplanetary atmospheres was given, along with the theory behind the aspects included in the simulator, and the relevant background knowledge was covered in Chapters 3-5. The simulator was presented with all its inputs and parameters, and a thorough walk-through of every module was given. Then, the modules and functions of the simulator were thoroughly tested with sensible inputs to validate their functionality. With the tests completed, it was concluded that all the modules work as intended.

After the test-phase was completed, a final “user-run” was conducted. Here, input parameters were externally supplied, including two input spectra of an intermediate-mass star with an exoplanet companion, along with other inputs based on actual scientific equipment. These included the quantum efficiency of a Teledyne E2V-4290 CCD and the Nordic Optical Telescope’s grism 10 of the ALFOSC instrument, among others. From this trial run, it became apparent that in order to observe the exoplanetary atmosphere with the given setup, the jitter of the system should be very well constrained. Such a system exists and was flown on the ASTERIA mission (Knapp et al. [2020]), where the achieved RMS of the pointing error was in the order of 1 arcsecond. In the trial run, it was determined that the jitter affected the resulting transmission spectrum quite heavily, both in terms of shape and position, but the effect was minimized in simulations with an enlarged PSF and an open slit. The final attempt in the trial case was done with these parameters, and it was concluded that the overall shape of the supplied exoplanetary atmosphere’s spectrum would be discernible, as would the largest spectral features, such as the sodium double line.

The aim of this thesis was to make and test a simulator for low-resolution spectroscopy. The Python-script HIDRA was created to serve this purpose, and all its functionalities and modules are concluded to work as intended.

This simulator can be implemented for use in the mission design for potential satellite missions and is especially relevant for missions searching for spectral features and trends of exoplanetary atmospheres.

Bibliography

The hitran database. Atomic and Molecular Physics Division, Harvard-Smithsonian Center for Astrophysics, <https://hitran.org/>.

M. Ackermann, M. Ajello, A. Allafort, L. Baldini, J. Ballet, et al. Detection of the characteristic pion-decay signature in supernova remnants. *Science*, 339(6121):807–811, 2013. ISSN 0036-8075. doi: 10.1126/science.1231160. URL <https://science.sciencemag.org/content/339/6121/807>.

George B. Airy. On the Diffraction of an Object-glass with Circular Aperture. *Transactions of the Cambridge Philosophical Society*, 5:283, January 1835.

L. Alminde, M. Bisgaard, I. Portillo, D. Smith, and L. Perez. Gomx-4: Demonstrating the building blocks of constellations, 2017.

Athem W. Alsabti and Paul Murdin. *Handbook of Supernovae*. Springer International Publishing, 2017. ISBN 978-3-319-21846-5. doi: 10.1007/978-3-319-21846-5_1. URL https://doi.org/10.1007/978-3-319-21846-5_1.

Jacob L. Bean, Jean-Michel Desert, Andreas Seifahrt, Nikku Madhusudhan, Igor Chilingarian, et al. Ground-based Transit Spectroscopy of the Hot-Jupiter WASP-19b in the Near-infrared. *The Astrophysical Journal*, 771(2):108, July 2013. doi: 10.1088/0004-637X/771/2/108.

Howard E. Bond, Gail H. Schaefer, Ronald L. Gilliland, Jay B. Holberg, Brian D. Mason, et al. "the sirius system and its astrophysical puzzles: Hubble space telescope and ground-based astrometry". *The Astrophysical Journal*, 840(2):70, May 2017. ISSN 1538-4357. doi: 10.3847/1538-4357/aa6af8. URL <http://dx.doi.org/10.3847/1538-4357/aa6af8>.

John C. D. Brand. *Lines of Light: The Sources of Dispersive Spectroscopy*. Gordon & Breach Publishers, 1st edition, 1995.

- Engineering Standardisation Board ESA. "ESA pointing error engineering handbook". ESSB-HB-E-003, ESA-ESTEC Requirements & Standards Division, 2011. Available at <http://peet.estec.esa.int/downloads/>, July 2011.
- M. Esposito and A. Zuccaro Marchi. In-orbit demonstration of the first hyperspectral imager for nanosatellites. In *International Conference on Space Optics – ICSO 2018*, volume 11180 of *Society of Photo-Optical Instrumentation Engineers (SPIE) Conference Series*, page 1118020, July 2019. doi: 10.1117/12.2535991.
- J. J. Fortney, M. Shabram, A. P. Showman, Y. Lian, R. S. Freedman, et al. Transmission Spectra of Three-Dimensional Hot Jupiter Model Atmospheres. *The Astrophysical Journal*, 709(2):1396–1406, February 2010. doi: 10.1088/0004-637X/709/2/1396.
- N. Yu Ganushkina, I. Dandouras, Y. Y. Shprits, and J. Cao. Locations of boundaries of outer and inner radiation belts as observed by cluster and double star. *Journal of Geophysical Research: Space Physics*, 116(A9), 2011. doi: 10.1029/2010JA016376. URL <https://agupubs.onlinelibrary.wiley.com/doi/abs/10.1029/2010JA016376>.
- Jonathan P. Gardner, John C. Mather, Mark Clampin, Rene Doyon, Matthew A. Greenhouse, et al. The James Webb Space Telescope. *Space Science Reviews*, 123(4):485–606, April 2006. doi: 10.1007/s11214-006-8315-7.
- Scott Gaudi, Sara Seager, Bertrand Mennesson, et al. Habitable exoplanet observatory final report, August 2019. Available at <https://www.jpl.nasa.gov/habex/documents/>.
- Thomas P. Greene, Laurie Chu, Eiichi Egami, Klaus W. Hodapp, Douglas M. Kelly, et al. Slitless spectroscopy with the james webb space telescope near-infrared camera (jwst nircam). *Space Telescopes and Instrumentation 2016: Optical, Infrared, and Millimeter Wave*, Jul 2016. doi: 10.1117/12.2231347. URL <http://dx.doi.org/10.1117/12.2231347>.
- F. Grundahl, T. Arentoft, J. Christensen-Dalsgaard, S. Frandsen, H. Kjeldsen, and P. K. Rasmussen. Stellar Oscillations Network Group SONG. In *Journal of Physics Conference Series*, volume 118 of *Journal of Physics Conference Series*, page 012041, October 2008. doi: 10.1088/1742-6596/118/1/012041.

A. P. Hatzes, W. D. Cochran, M. Endl, E. W. Guenther, S. H. Saar, G. A. H. Walker, S. Yang, M. Hartmann, M. Esposito, D. B. Paulson, and et al. Confirmation of the planet hypothesis for the long-period radial velocity variations of β geminorum. *Astronomy & Astrophysics*, 457(1):335–341, September 2006. ISSN 1432-0746. doi: 10.1051/0004-6361:20065445. URL <http://dx.doi.org/10.1051/0004-6361:20065445>.

Steve B. Howell. *Handbook of CCD Astronomy*. Cambridge University Press, 2nd edition, 2006.

Icko Iben and Alvio Renzini. Single star evolution i. massive stars and early evolution of low and intermediate mass stars. *Physics Reports*, 105(6):329 – 406, 1984. ISSN 0370-1573. doi: [https://doi.org/10.1016/0370-1573\(84\)90142-X](https://doi.org/10.1016/0370-1573(84)90142-X). URL <http://www.sciencedirect.com/science/article/pii/037015738490142X>.

Jr. Iben, I. The life and times of an intermediate mass star - In isolation/in a close binary. *Royal Astronomical Society, Quarterly Journal*, 26:1–39, March 1985.

John James. *The plane grating spectrograph*, page 63–88. Cambridge University Press, 2007. doi: 10.1017/CBO9780511534799.009.

James Janesick and Morley Blouke. Sky on a Chip: The Fabulous CCD. *Sky & Telescope*, 74:238, September 1987.

Amanda I. Karakas. *Low- and Intermediate-Mass Stars*, pages 461–481. Springer International Publishing, Cham, 2017. ISBN 978-3-319-21846-5. doi: 10.1007/978-3-319-21846-5_117. URL https://doi.org/10.1007/978-3-319-21846-5_117. eds.: Athem W Alsabti and Paul Murdin.

Rudolf Kippenhahn, Alfred Weigert, and Achim Weiss. *Evolution Through Helium Burning: Intermediate-Mass Stars*, pages 367–384. Springer Berlin Heidelberg, 2012. ISBN 978-3-642-30304-3. doi: 10.1007/978-3-642-30304-3_31. URL https://doi.org/10.1007/978-3-642-30304-3_31.

Quintus Kleipool, Antje Ludewig, Ljubiša Babić, Rolf Bartstra, Remco Braak, et al. Pre-launch calibration results of the TROPOMI payload on-board the Sentinel-5 Precursor satellite. *Atmospheric Measurement Techniques*, 11(12):6439–6479, December 2018. doi: 10.5194/amt-11-6439-2018.

- Mary Knapp, Sara Seager, Brice-Olivier Demory, Akshata Krishnamurthy, Matthew W. Smith, et al. Demonstrating High-precision Photometry with a CubeSat: ASTERIA Observations of 55 Cancri e. *The Astronomical Journal*, 160(1):23, July 2020. doi: 10.3847/1538-3881/ab8bcc.
- David G. Koch, William J. Borucki, Gibor Basri, Natalie M. Batalha, Timothy M. Brown, et al. Kepler Mission Design, Realized Photometric Performance, and Early Science. *The Astrophysical Journal*, 713(2):L79–L86, April 2010. doi: 10.1088/2041-8205/713/2/L79.
- C. Kouveliotou, E. Agol, N. Batalha, J. Bean, M. Bentz, et al. Enduring quests-daring visions (nasa astrophysics in the next three decades), 2014.
- Wiley J. Larson and James R. Wertz. *Space Mission Analysis and Design*. Microcosm, Inc., 2nd edition, 1992. ISBN 0-7923-1998-2.
- Kari Leppälä, Kirgiz Ssr, and Raimo Verkasalo. Protection of instrument control computers against soft and hard errors and cosmic ray effects, September 1989.
- Kevin L. Luhman. The Formation and Early Evolution of Low-Mass Stars and Brown Dwarfs. *Annual Review of Astronomy and Astrophysics*, 50:65–106, September 2012. doi: 10.1146/annurev-astro-081811-125528.
- Nikku Madhusudhan. Exoplanetary atmospheres: Key insights, challenges, and prospects. *Annual Review of Astronomy and Astrophysics*, 57(1):617–663, August 2019. ISSN 1545-4282. doi: 10.1146/annurev-astro-081817-051846. URL <http://dx.doi.org/10.1146/annurev-astro-081817-051846>.
- Michel Mayor and Didier Queloz. A Jupiter-mass companion to a solar-type star. *Nature*, 378(6555):355–359, November 1995. doi: 10.1038/378355a0.
- Carl E. McIlwain. Coordinates for mapping the distribution of magnetically trapped particles. *Journal of Geophysical Research*, 66(11):3681–3691, 1961. doi: 10.1029/JZ066i011p03681. URL <https://agupubs.onlinelibrary.wiley.com/doi/abs/10.1029/JZ066i011p03681>.
- Piyush M. Mehta, Andrew Walker, Earl Lawrence, Richard Linares, David Higdon, and Josef Koller. Modeling satellite drag coefficients

- with response surfaces. *Advances in Space Research*, 54(8):1590 – 1607, 2014. ISSN 0273-1177. doi: <https://doi.org/10.1016/j.asr.2014.06.033>. URL <http://www.sciencedirect.com/science/article/pii/S027311771400413X>.
- J. Nieke and M. Rast. Towards the copernicus hyperspectral imaging mission for the environment (chime). In *IGARSS 2018 - 2018 IEEE International Geoscience and Remote Sensing Symposium*, pages 157–159, 2018. doi: 10.1109/IGARSS.2018.8518384.
- F.L. Pedrotti, L.M. Pedrotti, and L.S. Pedrotti. *Introduction to Optics*. Cambridge University Press, 3rd edition, 2017. ISBN 9781108428262. URL https://books.google.dk/books?id=06o_DwAAQBAJ.
- F. Pepe, S. Cristiani, R. Rebolo, N. C. Santos, H. Dekker, et al. ESPRESSO@VLT – On-sky performance and first results. *arXiv e-prints*, art. arXiv:2010.00316, October 2020.
- Gert Raskin, Tjorven Delabie, Wim De Munter, Hugues Sana, Bart Vandenbussche, et al. Cubespec: low-cost space-based astronomical spectroscopy. In Makenzie Lystrup, Howard A. MacEwen, Giovanni G. Fazio, Natalie Batalha, Nicholas Siegler, and Edward C. Tong, editors, *Space Telescopes and Instrumentation 2018: Optical, Infrared, and Millimeter Wave*, volume 10698, pages 1639 – 1650. International Society for Optics and Photonics, SPIE, 2018. doi: 10.1117/12.2314074. URL <https://doi.org/10.1117/12.2314074>.
- Donald V. Reames. The Two Sources of Solar Energetic Particles. *Space Science Reviews*, 175(1-4):53–92, June 2013. doi: 10.1007/s11214-013-9958-9.
- George R. Ricker, Joshua N. Winn, Roland Vanderspek, David W. Latham, Gaspar. A. Bakos, et al. Transiting Exoplanet Survey Satellite (TESS). In Jr. Oschmann, Jacobus M., Mark Clampin, Giovanni G. Fazio, and Howard A. MacEwen, editors, *Space Telescopes and Instrumentation 2014: Optical, Infrared, and Millimeter Wave*, volume 9143 of *Society of Photo-Optical Instrumentation Engineers (SPIE) Conference Series*, page 914320, August 2014. doi: 10.1117/12.2063489.
- Peter Schneider. *Extragalactic Astronomy and Cosmology*. Springer-Verlag Berlin Heidelberg, 2nd edition, 2006. ISBN 10.1007/978-3-642-54083-7.

- Matthew W. Smith, Mary Knapp, Sara Seager, Christopher Pong, Amanda Donner, et al. Asteria: A cubesat enabling high precision photometry in a small package, July 2018. 42nd COSPAR Scientific Assembly 2018, Pasadena, California, July 14-22, <http://hdl.handle.net/2014/50225>.
- H. Strese and L. Maresi. Technology developments and status of hyperspectral instruments at the European Space Agency. In Steven P. Neeck, Philippe Martimort, and Toshiyoshi Kimura, editors, *Sensors, Systems, and Next-Generation Satellites XXIII*, volume 11151, pages 134 – 145. International Society for Optics and Photonics, SPIE, 2019. doi: 10.1117/12.2533129. URL <https://doi.org/10.1117/12.2533129>.
- James A. van Allen and Louis A. Frank. Radiation Around the Earth to a Radial Distance of 107,400 km. *Nature*, 183(4659):430–434, February 1959. doi: 10.1038/183430a0.
- Joshua N. Winn. Transits and Occultations. *arXiv astro-ph*, art. arXiv:1001.2010, January 2010.
- William H. Wollaston. A method of examining refractive and dispersive powers, by prismatic reflection. *Philosophical Transactions of the Royal Society*, 92:365, 380, December 1802.

